



Computational modeling of the large deformation and flow of viscoelastic polymers

Tong Shen¹ · Rong Long¹ · Franck Vernerey¹

Received: 20 April 2018 / Accepted: 2 August 2018
© Springer-Verlag GmbH Germany, part of Springer Nature 2018

Abstract

Deformation of soft polymeric materials often involves complex nonlinear or transient mechanical behaviors. This is due to the dynamic behaviors of polymer chains at the molecular level within the polymer network. In this paper, we present a computational formulation to describe the transient behavior (e.g., viscoelasticity) of soft polymer networks with dynamic bonds undergoing large to extreme deformation. This formulation is based on an Eulerian description of kinematics and a theoretical framework that directly connects the molecular-level kinetics of dynamic bonds to the macroscopic mechanical behavior of the material. An extended finite element method is used to discretize the field variables and the governing equations in an axisymmetric domain. In addition to validating the framework, this model is used to study how the chain dynamics affect the macroscopic response of material as they undergo a combination of flow and elasticity. The problems of cavitation rheology and polymer indentation under extreme deformation are investigated in this context.

1 Introduction

Many industrial applications and scientific research rely on the development of polymeric materials whose mechanical behaviors lie between that of a nonlinear elastic solid to that of a purely viscous fluid. For instance, in the field of adhesives, the polymer must have the ability to flow within the small cavities of a materials surface to create strong bonding after curing [26,28]. 3D printing (additive manufacturing) technique has also caught more and more attention since it provides a simple approach to fabricate different structures with good accuracy. The main challenge to increase the resolution of this technique is the requirement to accurately control the material deposition and subsequent curing [29,31]. Additive manufacturing is another industrial application where a fine control of polymer viscoelasticity is needed. Indeed, the way by which a new material layer is deposited during 3D printing is determined by the combined flow and elasticity of the uncured polymer [10,43].

There is therefore a strong need to accurately model and predict the combination of elastic stresses, viscous flow and continuous changes in material properties occurring during

these processes. Numerical modeling developed based on viscoelastic material models has therefore become an attractive tool to understand and eventually control the process but unfortunately has been hindered by two main obstacles: first, from a numerical stand-point, the existence of extremely large deformations ($>> 100\%$) that cannot be easily handled with traditional Lagrangian finite element approaches. Second, theoretical-wise, a lack of connection between the molecular physics to macroscopic mechanical behavior.

The viscoelasticity of polymers has been theoretically studied over the past decades. However, most existing models are either phenomenological (e.g., linear Maxwell or Kelvin-Voigt model [14]) or based on continuum level elastic models (e.g., Neo-Hookean [60], Arruda-Boyce [8] or Holzapfel model [35]). One common issue for these models is a lack of connection between the change in the network structure of the polymer, its physical properties and the resulting flow and elastic stresses driving the rheology of materials. Besides, these models rely on the definition of Lagrangian strain and the concept of reference configuration to describe material deformation. When it comes to modeling the rheology of materials involving very large deformation ($>> 100\%$), their implementations may therefore be challenging. Miehe and Goktepe [49,50] further developed a micro-sphere model to link the stretch of molecular chains and polymer response. In this model, the micro-mechanics of a chain is characterized by a micro-tube that captures its end-to-end distance.

✉ Franck Vernerey
Franck.Vernerey@colorado.edu

¹ Mechanical Engineering, University of Colorado Boulder,
1111 Engineering Drive, Boulder, CO 80309-0427, USA

The macroscopic response of the polymer network is then obtained by homogenizing the micro-state variables on an unit sphere that describes the chain orientation in 3D. However, this theory can only be applied to describe the behavior of static (i.e., covalent) networks, where the viscoelasticity is caused by the reptation of entangled chains. More effort is needed to generalize this theory to describe the behavior of physical networks, where the viscoelasticity results from the breakage and reformation of physical cross-links [2]. A solution to these issues can potentially be provided by statistical approaches, such as the transient network theory (TNT), [66,70,74,78], that establishes a bridge between polymer chain configuration and the stress in the network. As discussed recently in [74], it particularly has the following advantages from a practical viewpoint. First, it is able to clearly connect the molecular mechanisms at the level of polymer chains (entanglement [15], reptation [16] and the breaking and reforming of physical bonds (i.e. ionic bonds)) to the macroscopic response of the network. This presents a departure from the more phenomenological viscoelastic models such as the Maxwell and Kelvin-Voigt models [39,47,57]. Second, the TNT relies on a statistical distribution of the polymer chain and is therefore completely independent from the definition of a Lagrangian strain and the reference configuration. Despite these advantages, it has not, to date, been the object of a numerical implementation to predict the behavior of visco-elastic polymers.

In this paper, we therefore proposed a computational framework, based on the TNT, that can be used to predict the deformation of soft polymers ranging from a purely elastic solid to a viscoelastic fluid, irrespective of the level of deformation. Traditionally, the computational solid mechanics has followed a Lagrangian approach due to the existence of a reference configuration about which to define strain measures. When large deformations occur, traditional methods however suffer from the fact that Lagrangian elements can be significantly distorted, deteriorating the approximation accuracy of the numerical scheme. Although many strategies have been elaborated to address this issue, such as remeshing via interpolation techniques between old and new meshes [46,56], they are cumbersome and subjected to numerical errors due to the need for intensive interpolations. An alternative to handle large deformation is to use the Deforming-Spatial-Domain/Space-Time formulation [67], which introduces a remapping process after a deformation step on Lagrangian mesh is completed. The remapping helps reduce the frequency of remeshing during large deformation, and thus can reduce the interpolation errors. Although this method was shown to be robust in handling problems involving moving boundaries and finite deformations, it still relies on the existence of a reference configuration. When it comes to modeling the rheology of materials involving extreme deformation,

its implementation may be challenging and the range of deformation is limited.

In contrast, Eulerian descriptions are traditionally used for fluids due to their lack of a reference configuration. Compared to Lagrangian formulation, the advantage of Eulerian formulation is its capacity to handle arbitrary deformation, regardless of magnitude [7,18]. Several studies have adopted the Eulerian descriptions for modeling hyperelastic materials, such as the work by Plohr and Sharp [54], as well as Duddu et al. [20]. Besides, numerical models have also been proposed to describe the rheology of viscoelastic materials, most of which are based on the Arbitrary Lagrangian–Eulerian (ALE) scheme [18,65]. In this scheme, the computational mesh can move in a pre-defined manner in order to optimize the shape of the elements [18]. Using this methodology, many studies have focused on modeling the viscoelastic flow under different conditions [21,33,36]. When using an Eulerian formulation to model solids, one main issue pertains to the handling of moving material boundaries on the underlying mesh. This requires the development of boundary conditions based on a moving surface (for instance using the levelset method [24,62,64,75]). In addition, field variables are usually discontinuous across the boundary, requiring special numerical treatments. Notably, Choi et al. employed the Extended Finite Element Method (XFEM) in combination with ALE, and modeled the behavior of viscoelastic particulate flows under various conditions [11–13]. However, these numerical schemes still rely on a deforming mesh to track the material deformation. When modeling the large or extreme deformations, these methods still need remeshing from time to time to alleviate mesh distortions. To eliminate this problem, Foucard et al. [25] developed a coupled Eulerian–Lagrangian (CEL) formulation, which eliminates the deforming mesh by characterizing the material deformation using Lagrangian particles on the fixed Eulerian mesh. This formulation has shown to be powerful for modeling the large or even extreme deformation of hyperelastic materials.

In this paper, we build upon the work of Foucard et al. [25] to construct a coupled Eulerian Lagrangian (CEL) implementation of the TNT to describe the extreme deformation of viscoelastic soft polymers. In this formulation, momentum equations and transport equations are solved in a staggered manner in time in the Eulerian framework and the tracking of the interface motion is achieved by employing the Particle-based Moving Interface Method (PMIM) [27]. We show that this scheme is accurate for extreme deformation and viable for connecting the microscopic physics to the macroscopic transient behaviors of materials. The manuscript is organized as follows. In Sect. 2, we review the main elements of the TNT to model the response of dynamic polymer networks. In Sect. 3, we present the numerical strategy to discretize the weak form, the tracking of the interface and the Lagrangian

transport of the variable fields, along with benchmark problems to verify the method. In Sect. 4, we investigate the mechanics of dynamic polymer networks and how it evolves through two numerical examples: cavitation rheology and indentation of a spherical particle. Finally, Sect. 5 provides a short discussion and concluding remarks.

2 Review of the transient network theory (TNT) for viscoelastic polymers

In this section, we briefly review the TNT previously introduced in [70]. We concentrate here on polymers with long chains that are in a coil state and never straightened. The chain end-to-end distances, defined by the distances between two crosslinks, follow the Gaussian statistics and the association and dissociation kinetics are independent of the force sustained by the chain.

2.1 Mechanics of polymer network with dynamic chains

Let us consider an incompressible polymer network consisting of linear chains of density C , where C is the number of chains per unit volume, that are connected to each other to form a network. The network is assumed to be dynamic, wherein the polymer chains associate and dissociate over time at a rate of k_a and k_d , respectively (Fig. 1). The first step in the TNT is to describe the chain population by a distribution function $\phi(\mathbf{r}, t)$ that classifies chains according to their end-to-end vector \mathbf{r} and to determine how the population is affected by the deformation history and the rates k_a and k_d .

2.1.1 Statistical description of polymer networks

The mechanical response of a polymer can be described by the states of the chains and their contribution to the overall response of the network. For an initially isotropic network, the chains span all possible directions and we can use the end-to-end vector to represent their directions (e.g., by the

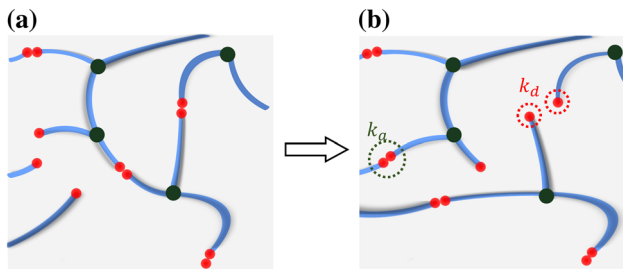


Fig. 1 Schematic representation of dynamic bonds in a polymer network, where dissociation and re-association happen with rates of k_d and k_a , respectively

polar angle θ and azimuthal angle ω in the spherical coordinates) and length $r = |\mathbf{r}|$. The mechanics of the network may then be understood through a statistical description of the end-to-end configuration of all polymer chains within a continuum point. Here, we use a chain distribution function $\phi(\mathbf{r}) = \phi(r, \theta, \omega)$ to describe the chain population. This distribution can be captured by two key quantities: density c of attached chains (i.e., those that are connected to the network) and the so-called chain distribution tensor defined as

$$c = \int_{\Omega} \phi(\mathbf{r}) d\Omega \quad (1)$$

$$\boldsymbol{\mu}(t) = \frac{1}{c} \int_{\Omega} \phi(\mathbf{r}) \mathbf{r} \otimes \mathbf{r} d\Omega. \quad (2)$$

The tensor $\boldsymbol{\mu}$ represents, in an average sense, the stretch experienced by chains in the network. At the stress-free state, the end-to-end distance of the chains are assumed to follow the Gaussian distribution. In this case, the distribution tensor becomes the identity tensor $\boldsymbol{\mu}_0 = \mathbf{I}$ [74].

2.1.2 Evolution equations

To determine how the chain distribution changes with time, let us consider a small material volume experiencing deformation over time. At a given time, this deformation can be expressed by the velocity gradient $\mathbf{L} = \nabla \mathbf{v}$ where: $\mathbf{v} = \mathbf{v}(\mathbf{x}, t)$ is the velocity of a point located at \mathbf{x} at a given time t . If we assume that the chains undergo affine deformation (i.e. their deformation follow the macroscopic deformation \mathbf{L}), it is possible to construct an evolution equation for the chain distribution ϕ if the rates of chain association and dissociation are known [74]. Using an appropriate average over the chain population, we have shown that the evolution equation for the chain distribution tensor takes the form

$$\dot{\boldsymbol{\mu}} = k_a \left(\frac{C - c}{c} \right) \boldsymbol{\mu}_0 - k_d \boldsymbol{\mu}. \quad (3)$$

Assuming the polymer network is initially in its stress-free state, the initial condition for this differential equation is $\boldsymbol{\mu}(t = 0) = \boldsymbol{\mu}_0$ [74]. The left hand side of the above equation is the objective Truesdell rate of the distribution tensor $\dot{\boldsymbol{\mu}} = \dot{\boldsymbol{\mu}} - (\mathbf{L}\boldsymbol{\mu} + \boldsymbol{\mu}\mathbf{L}^T)$. We note here that this equation already incorporates the assumption of incompressibility, i.e. $\text{tr}(\mathbf{L}) = \nabla \cdot \mathbf{v} = 0$. The term on the left-hand side of Eq. (3) captures the change in the chains configuration due to macroscopic deformation. The right-hand side shows the evolution of $\boldsymbol{\mu}$ due to the chain dynamics. The first term describes the association of polymer chains to their natural state and the second term describes the dissociation of chains in their current (stressed) state. As discussed in [74], the values of k_a and k_d may be sensitive to external factors such as temperature or chemical environment. While this may be considered for

specific problems, in this paper, we assume they are both constants for simplicity. Under this consideration, the dynamics of chains degenerates to the bond exchange reaction such that $k_a(C - c) = k_dc$ [74] and Eq. (3) takes a simpler form

$$\dot{\boldsymbol{\mu}} = k_d(\boldsymbol{\mu}_0 - \boldsymbol{\mu}). \quad (4)$$

To further investigate the effect of chain dynamics, let us consider the situation where the deformation is frozen (i.e., $\mathbf{L} = \mathbf{0}$) at a given time t_1 . In this case, Eq. (4) becomes $\dot{\boldsymbol{\mu}} = k_d(\boldsymbol{\mu}_0 - \boldsymbol{\mu})$, which lends a solution of the form $\boldsymbol{\mu}(t) = \boldsymbol{\mu}_0 + [\boldsymbol{\mu}(t_1) - \boldsymbol{\mu}_0]e^{-k_d(t-t_1)}$. We therefore see that the distribution tensor relaxes towards its stress-free state $\boldsymbol{\mu}_0$ with characteristic time $\tau = 1/k_d$.

We note that, in this paper, the proposed theory describes the dynamics of the polymer with two constant $k_a = k_d$. These two constants may further be connected to the physics and interaction of the chains, which could be from purely kinetic nature (physical cross-links, covalent adaptable networks), or physical nature such as in the presence of entanglements. In the latter case, the constant k_a and k_d arise from the disruption of entanglements and reptation of long polymer chains during deformation. In other words, an entangled chain may appear as mechanically active at short times, since entanglements may themselves be viewed as physical cross-links. However, as the chain is stretched, over time, it will dissociate from the entanglement and evolve towards a more relaxed configuration. This new configuration may contain new entanglement points, whose appearance can be interpreted as an attachment event. Such molecular mechanisms have been captured by the reptation theory of de Gennes [15], in which the lifetime of a physical link was found to scale with the square of chain length. The rate of detachment may therefore be seen as the inverse of this lifetime, i.e., $k_a = k_d = 1/\tau$.

2.1.3 Energy aspects and the stress tensor

Here, we provide the link between the statistical description of chains and the macroscopic mechanical quantities, including the stored elastic energy, the dissipation energy and the stress tensor. This is accomplished through the difference in elastic stored energy $\Delta\Psi_e$ between the current and the stress-free state, whose form can be written in terms of the chain distribution as

$$\Delta\Psi_e = \frac{ck_BT}{2} \text{tr}(\boldsymbol{\mu} - \boldsymbol{\mu}_0) + p \left(\frac{C}{C_0} - 1 \right). \quad (5)$$

In this equation, k_BT is the thermal energy and p is a Lagrange multiplier that enforces the material's incompressibility condition $C/C_0 - 1 = 0$ with C_0 the density of chains at the initial time. Here, we evaluate the change in

energy when the polymer undergoes a macroscopic deformation, characterized by the velocity gradient \mathbf{L} . For the sake of simplicity, we here consider an iso-thermal process while a more general study was introduced in [74]. Under the iso-thermal condition, according to the second principle of thermodynamic, the dissipation energy can be obtained from the difference between the work done by the internal force and the change in the stored elastic energy as

$$\mathcal{D} := \boldsymbol{\sigma} : \mathbf{L} - \Delta\dot{\Psi}_e \geq 0 \quad (6)$$

where $\boldsymbol{\sigma}$ is the Cauchy stress tensor. We note that the rate of change in stored elastic energy can be further written as (see detailed derivations in ‘‘Appendix 1’’)

$$\Delta\dot{\Psi}_e = [ck_BT(\boldsymbol{\mu} - \boldsymbol{\mu}_0) + p\mathbf{I}] : \mathbf{L} - k_d \frac{ck_BT}{2} \text{tr}(\boldsymbol{\mu} - \boldsymbol{\mu}_0). \quad (7)$$

Using this expression, Eq. (6) can be rewritten as

$$\begin{aligned} \mathcal{D} &:= [\boldsymbol{\sigma} - ck_BT(\boldsymbol{\mu} - \boldsymbol{\mu}_0) - p\mathbf{I}] : \mathbf{L} - k_d \frac{k_BT}{2} \text{tr}(\boldsymbol{\mu} - \boldsymbol{\mu}_0) \\ &\geq 0. \end{aligned} \quad (8)$$

Assuming that the first term on the right-hand side of Eq. (8) vanishes and the second term verifies the inequality, the expression for the Cauchy stress is then identified as

$$\boldsymbol{\sigma} = ck_BT(\boldsymbol{\mu} - \boldsymbol{\mu}_0) + p\mathbf{I}. \quad (9)$$

When the network is static ($k_a = k_d = 0$) and incompressible, it is shown in [74] that the distribution tensor coincides with the left Cauchy–Green tensor $\boldsymbol{\mu} = \mathbf{F}\mathbf{F}^T$, where \mathbf{F} is the deformation gradient tensor. In this case, Eq. (7) and (9) degenerate to the expressions for the neo-Hookean model in classical rubber elasticity [34]. In addition, the energy dissipation takes the form

$$\mathcal{D} = k_d \frac{k_BT}{2} \text{tr}(\boldsymbol{\mu} - \boldsymbol{\mu}_0). \quad (10)$$

This quantifies the strain energy release rate in the network due to chain detachment in the stressed state.

2.1.4 Physical states of the network

Because this description enables a clear connection between macroscopic and molecular scales, a few relevant measures of the physical state of the network can be recovered by the TNT. First, defining the stretch of the end-to-end vector of a chain as $\lambda = \mathbf{r}/\sqrt{N}b$, the root mean square of chain stretch

λ_{rms} can be extracted from the distribution tensor as follows

$$\lambda_{rms} = \sqrt{\frac{1}{c} \int_{\Omega} \phi(\lambda) \lambda \cdot \lambda d\Omega} = \sqrt{\frac{tr(\boldsymbol{\mu})}{3}}. \quad (11)$$

Second, the average orientation of chains can be characterized by the average chain angle γ as

$$\gamma = \arccos \left(\sqrt{\frac{\mathbf{n} \cdot (\boldsymbol{\mu} \mathbf{n})}{tr(\boldsymbol{\mu})}} \right) \quad (12)$$

where \mathbf{n} is an arbitrary unit vector and the angle γ is the average chain angle with respect to the direction specified by \mathbf{n} .

2.2 Field equations

Let us now discuss the governing equations associated with the problem of a continuum polymer body deforming non-uniformly under the action of external forces. For this, we represent the body as a three-dimensional domain Ω^s bounded by a smooth boundary Γ . In this paper, we consider overdamped systems, in which inertial effects are negligible [58]. Therefore, the balance of momentum reads [34]

$$\nabla \cdot \boldsymbol{\sigma} + \mathbf{b} = \mathbf{0} \quad \text{in } \Omega^s \quad (13)$$

where \mathbf{b} is the body force per unit volume in the current configuration. To relate the stress to macroscopic deformation through Eq. (9) and evolution equation (3), the problem can be equivalently considered as an initial value problem, where stress-free condition with zero body force and external loading is considered at the initial state

$$\boldsymbol{\sigma}(t=0) = \mathbf{0} \quad \text{in } \Omega^s(0).$$

Since the evolution of the network is incremental by nature, it is convenient to similarly recast the governing equation in their incremental form as

$$\begin{aligned} \nabla \cdot \dot{\boldsymbol{\sigma}} + \dot{\mathbf{b}} &= \mathbf{0} \quad \text{in } \Omega^s \\ \nabla \cdot \mathbf{v} &= 0 \quad \text{in } \Omega^s \end{aligned} \quad (14)$$

where the first term can be further written $\nabla \cdot \dot{\boldsymbol{\sigma}} = ck_B T \nabla \cdot \dot{\boldsymbol{\mu}} + \nabla \dot{p}$ according to Eq. (9). Besides, the above equations are subjected to boundary conditions that read

$$\begin{aligned} \mathbf{v} &= \bar{\mathbf{v}} \quad \text{on } \Gamma_D \\ \mathbf{n} \cdot \dot{\boldsymbol{\sigma}} &= \dot{\mathbf{t}} \quad \text{on } \Gamma_N. \end{aligned} \quad (15)$$

The symbols Γ_D and Γ_N are the Dirichlet and Neumann parts of Γ for the boundary conditions for velocity and traction, respectively. In the remainder of this paper, we consider

geometries that have an axis of symmetry and therefore formulate the above equations in a cylindrical coordinate system $\mathbf{x} = \rho \hat{\mathbf{e}}_\rho + z \hat{\mathbf{e}}_z$ where $\hat{\mathbf{e}}_\rho$ and $\hat{\mathbf{e}}_z$ are the orthonormal basis vectors. The components of Eq. (14) along the $\hat{\mathbf{e}}_\rho$ and $\hat{\mathbf{e}}_z$ directions are given in “Appendix 2”.

3 Numerical solution strategy

The objective of this section is to introduce a numerical strategy to solve the above field equations. Because dynamic polymers can experience levels of deformation ranging from those of an elastic solid (limited) to those of a fluid (extreme), we specifically choose a numerical scheme that couples the Eulerian and updated Lagrangian formulations, combined with an evolution scheme for the material interface Γ on a fixed Eulerian mesh. The solution strategy at each time increment (denoted by time t_n) can be summarized as follows: the velocity field \mathbf{v} and the change in pressure field \dot{p} are computed from Eq. (14) in the current domain $\Omega^s(t_n)$ using the extended Finite Element Method (XFEM). Using the velocity field, the material interface $\Gamma(t_n)$ is then updated to its next configuration $\Gamma(t_{n+1})$ by the Particle-based Moving Interface Method (PMIM) [25]. For each point in the new material domain bounded by $\Gamma(t_{n+1})$, the field variables $\boldsymbol{\mu}$ and p are transported using an explicit updated Lagrangian mapping scheme. A more detailed description of each step will be presented in the following sections.

We note here that, for moving boundary problems, the interface Γ usually does not coincide with the mesh and the boundary conditions cannot be directly enforced on the grid nodes. While the Neumann boundary condition can still be straightforwardly applied along Γ_N by interpolations, directly imposing the Dirichlet boundary condition is more difficult because one needs to specify all the degrees of freedom in the elements that are cut by Γ_D . This is usually cumbersome and may cause problems such as poor convergence rates [51]. In this paper, to circumvent this difficulty, we choose to apply the Dirichlet constraints via the Lagrange multiplier method for which a detailed discussion can be found in [26,51].

3.1 Extended finite element method

To construct the weak form of the finite element formulation, we first introduce the arbitrary test functions $\boldsymbol{\omega}_v$ in \mathcal{V} , ω_p in \mathcal{P} and ω_λ in \mathcal{L} where \mathcal{V} , \mathcal{P} and \mathcal{L} are the admissible spaces for velocity, rate of change in pressure, and Lagrange multiplier that enforces the velocity $\mathbf{v} = \bar{\mathbf{v}}$ on Γ_D respectively. By multiplying Eq. (14) with the test functions and integrating it over the numerical domain Ω^s , the problem consists of finding the velocity field \mathbf{v} , change in pressure field \dot{p} and the Lagrange multiplier field λ in the domain such that for arbitrary

trary ω_v, ω_p and ω_λ , the following equations (corresponding to Eq. (14)) are satisfied in Ω^s

$$\begin{aligned} & -ck_B T \int_{\Omega^s} \nabla \omega_v \dot{\mathbf{u}} \, d\Omega^s - \int_{\Omega^s} \nabla \omega_v \dot{p} \, d\Omega^s \\ & + \int_{\Omega^s} \omega_v \dot{\mathbf{b}} \, d\Omega^s + \int_{\Gamma_N} \omega_v \dot{\mathbf{t}} \, d\Gamma_N \\ & + \int_{\Gamma_D} \omega_v \lambda \, d\Gamma_D = 0 \\ & \int_{\Omega^s} \omega_p (\nabla \cdot \mathbf{v}) \, d\Omega^s = 0 \\ & \int_{\Gamma_D} \omega_\lambda (\mathbf{v} - \bar{\mathbf{v}}) \, d\Gamma_D = 0. \end{aligned} \quad (16)$$

where we note that the fields \mathbf{v} and \dot{p} are continuous in Ω^s while discontinuous across Γ , and the field λ is continuous on Γ_D .

Although the problem is three dimensional (3D), only 2D discretization of Eq. (16) is required to solve an axisymmetric problem. Here, to ensure the stability of the solution, we adopt a mixed formulation [80], wherein the velocity field \mathbf{v} is interpolated with nine-node (biquadratic) element shape function and the change in pressure \dot{p} is interpolated with four-node (bilinear) element shape function. Since the mesh is structured and does not conform with the material interface Γ , we here use the zero-level of a levelset function $\phi(\mathbf{x})$ to describe the position of Γ , where $\phi(\mathbf{x})$ is defined as the signed distance function from it [52]. In elements that do not intersect with Γ , the variables \mathbf{v} and \dot{p} are interpolated using the standard finite element method (FEM). However, for an element e that is cut by Γ , we employ the XFEM where additional interpolation functions are introduced to account for the discontinuities across Γ [64]. With this formalism, the interpolations of the velocity and pressure fields are written

$$\begin{aligned} v_i(\mathbf{x}, t) &= \sum_{l=1}^9 N_9^l(\mathbf{x}) v_i^l(t) \\ &+ \sum_{l=1}^9 N_9^l(\mathbf{x}) \left(H(\phi(\mathbf{x}) - H(\phi(\mathbf{x}^l))) \right) \hat{v}_i^l(t) \\ \dot{p}(\mathbf{x}, t) &= \sum_{l=1}^4 N_4^l(\mathbf{x}) \dot{p}^l(t) \\ &+ \sum_{l=1}^4 N_4^l \left(H(\phi(\mathbf{x}) - H(\phi(\mathbf{x}^l))) \right) \hat{\dot{p}}^l(t) \end{aligned} \quad (17)$$

where N_9 and N_4 are the 2-D regular quadratic and linear shape functions. The superscript index l is used for node numbering and the subscript indices i is used for numbering the cylindrical coordinate components; the terms \hat{v}_i^l and $\hat{\dot{p}}^l$ are the enriched unknowns of velocity and change in pressure

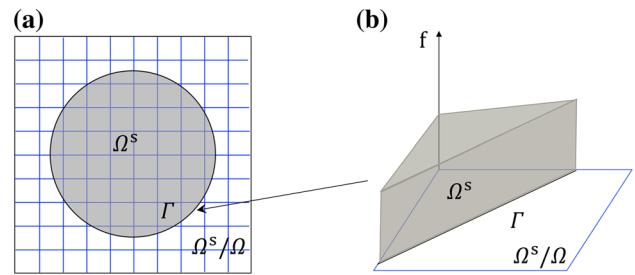


Fig. 2 **a** Schematic of the discretized domain. The interface splits some elements and results in discontinuities in these elements. **b** The discontinuity of quantity f in the split elements, where f could be the components of velocity \mathbf{v} or change in pressure \dot{p}

that describe the discontinuities at node l , as interpolated with the Heaviside function $H(\phi(\mathbf{x}))$. Besides, the Lagrange multiplier λ is interpolated by a 1-D linear shape function \bar{N} along the interface section Γ that is inside e

$$\lambda(\mathbf{x}, t) = \sum_{l=1}^2 \bar{N}^l(\mathbf{x}, t) \lambda^l(t).$$

To obtain a compact version of discretized equations, the interpolated fields are written in a vector form as

$$\begin{aligned} \mathbf{v}(\mathbf{x}, t) &= \mathbf{N}_v \cdot \mathbf{v}^e(t) \\ \dot{p}(\mathbf{x}, t) &= \mathbf{N}_p \cdot \dot{\mathbf{p}}^e(t) \\ \lambda(\mathbf{x}, t) &= \bar{\mathbf{N}} \cdot \lambda^e(t). \end{aligned} \quad (18)$$

In the equation, the nodal velocity is expressed by $\mathbf{v}^e = \{v_\rho^1, v_z^1, \dots, v_\rho^9, v_z^9, \hat{v}_\rho^1, \hat{v}_z^1, \dots, \hat{v}_\rho^9, \hat{v}_z^9\}_{36 \times 1}^T$. Similarly, the nodal values of pressure are expressed by $\dot{\mathbf{p}}^e = \{\dot{p}^1, \dots, \dot{p}^4, \hat{\dot{p}}^1, \dots, \hat{\dot{p}}^4\}_{8 \times 1}^T$, where the terms \hat{v}^l and $\hat{\dot{p}}^l$ represent the enriched degrees of freedom that accounts for the discontinuities across the interface (Fig. 2). Besides, the nodal values of Lagrange multiplier read $\lambda^e = \{\lambda^1, \lambda^2\}_{2 \times 1}^T$. The detailed expressions for the shape functions \mathbf{N}_v , \mathbf{N}_p and $\bar{\mathbf{N}}$ are given in “Appendix 3”.

Substituting these interpolations into the weak form (16) and after further derivations, the discretized governing equation takes the following matrix form

$$\begin{bmatrix} \mathbf{K}_{vv} & \mathbf{K}_{vp} & \mathbf{K}_{v\lambda} \\ \mathbf{K}_{pv} & \mathbf{0} & \mathbf{0} \\ \mathbf{K}_{\lambda v} & \mathbf{0} & \mathbf{0} \end{bmatrix} \begin{bmatrix} \mathbf{v} \\ \dot{\mathbf{p}} \\ \lambda \end{bmatrix} = \begin{bmatrix} \mathbf{f}_v \\ \mathbf{0} \\ \mathbf{f}_\lambda \end{bmatrix}. \quad (19)$$

For clarity, we provide expressions for each of the above submatrices in “Appendix 4”. We further note that the matrix shown in Eq. (19) is symmetric and sparse, it can thus be solved using the *LU* factorization method embedded in UMF-PACK library of Matlab.

3.2 Stability test: the LBB (inf–sup) condition

The mixed finite element discretization introduced above must satisfy the so-called LBB (or inf–sup) condition [3,4] to ensure its stability and solvability. Here, we focus on evaluating the v/\dot{p} formulation, since the condition for the Lagrange multipliers λ has been evaluated in [51]. For our problem, this condition imposes that there exists a positive constant γ (independent of the element size h) called the inf–sup value such that

$$\inf_{\omega_p^h \in \dot{\mathcal{P}}^h} \sup_{v^h \in \mathcal{V}^h} \frac{\int_{\Omega} \omega_p^h \nabla \cdot \mathbf{v}^h d\Omega}{\|\mathbf{v}^h\|_{H^1} \|\omega_p^h\|_{L^2}} \geq \gamma > 0 \quad (20)$$

where $\dot{\mathcal{P}}^h$ and \mathcal{V}^h are the finite element subspaces $\dot{\mathcal{P}}^h \subset \dot{\mathcal{P}}$ and $\mathcal{V}^h \subset \mathcal{V}$, corresponding to the discretized test function ω_p^h and velocity \mathbf{v}^h . The subscripts H^1 and L^2 indicates the H^1 sobolev norm and the L^2 norm, respectively. According to [4], the above equation can be equivalently written in terms of the submatrix \mathbf{K}_{pv} in Eq. 19 as

$$\inf_{\dot{\mathcal{P}}^h} \sup_{\mathcal{V}^h} \frac{\mathbf{W}_h^T \mathbf{K}_{pv} \mathbf{V}_h}{[\mathbf{V}_h^T \mathbf{S}_h \mathbf{V}_h]^{1/2} [\mathbf{W}_h^T \mathbf{K}_{pv} \mathbf{W}_h]^{1/2}} \geq \gamma > 0 \quad (21)$$

where \mathbf{W}_h and \mathbf{V}_h are vectors of the nodal values corresponding to ω_p^h and \mathbf{v}^h , and \mathbf{S}_h is the matrix corresponding to the norm operator $\|\cdot\|_{H^1}$ computed according to [3]. This problem can be further degenerated to determining the inf–sup value $\gamma = \sqrt{(\lambda_k)}$, where λ_k is the smallest nonzero eigenvalue of the following equation

$$\mathbf{K}_{pv} \phi = \lambda_k \mathbf{S} \phi. \quad (22)$$

In order to pass the inf–sup condition, γ must be bounded away from zero when the mesh size h is decreased. In other words, the LBB condition is passed if the inf–sup value does not decrease towards zero as the mesh is refined. [9].

3.3 Tracking the motion of the interface

To track the evolution of the interface Γ , we use the particle-based moving interface method (PMIM) [25,41,59], where the interface is represented by particles whose spatial distribution remains quasi-uniform over time. To avoid repetition, we here summarize the main steps of the method; interested readers can find additional details in “Appendix 5”.

1. *Initialization* At the initial time t_0 , given the initial geometry of the interface Γ^0 , we gather the grid nodes whose distances to Γ^0 are smaller than a cut-off value d_0 . The particles with position vector \mathbf{y}^{t_0} are chosen as the normal projection of these nodes on the interface.

2. *Update* At any subsequent time t , given the velocity field \mathbf{v}^t , the new interface Γ^{t+dt} is obtained by evolving the particles at \mathbf{y}^t to their new positions \mathbf{y}^{t+dt} using a second order Runge-Kutta time integration scheme.
3. *Approximation* To approximate the geometry of Γ^{t+dt} , for each particle \mathbf{y}_p , collect the positions of the closest m particles within its neighborhood, and construct a polynomial $\mathbf{r}(\mathbf{y}_p, t + dt)$ of degree $n < m$.
4. *Update geometrical quantities* Compute the geometrical quantities of Γ^{t+dt} using $\mathbf{r}(\mathbf{y}_p, t + dt)$, including the normal vectors $\bar{\mathbf{n}}^{t+dt}$ and the levelset function $\phi(t + dt)$.
5. *Resample* To resample Γ^{t+dt} , we find the new grid nodes that are near the updated interface Γ^{t+dt} , and re-allocate particles via the projection operation used in step 1.

3.4 Lagrangian transport of μ and p

In this problem, two field variables, the chain distribution tensor μ and pressure p , are used to characterize the states (i.e., average chain stretch and energy dissipation) and the stress in the network. Although these two variables are not directly solved from the governing Eq. (14), their values are updated at each time step using \mathbf{v} and \dot{p} obtained from Eq. (19). For regular elements that are not split by the interface, the degrees of freedom can be directly transported using an updated Lagrangian scheme. However, the transport of μ and p in the split elements are more complicated because the interface $\Gamma(t)$ describing the material domain is moving from time to time. Therefore, in addition to transporting the regular degrees of freedom (DOF) of μ and p , we also need to update their enriched DOF to account for the discontinuities across $\Gamma(t)$. In order to handle this, we herein use a two-step scheme described in [25] to transport these two variables. In the first step, the regular DOF μ^{reg} , p^{reg} are updated as followed:

1. At time t , given the velocity solution \mathbf{v}^t , use the PMIM algorithm to update the material domain $\Omega^s(t)$ and the interface $\Gamma(t)$ to their new positions $\Omega^s(t + dt)$ and $\Gamma(t + dt)$.
2. For each node i in the updated domain $\Omega^s(t + dt)$, material points with coordinates \mathbf{x}_i^{t+dt} are backtracked to their position \mathbf{x}_i^t at time t , along with the variables \mathbf{v}_i^t and \dot{p}_i^t interpolated by the XFEM approximation. From this, the velocity gradient tensor at \mathbf{x}_i^t is computed by: $\mathbf{L}_i^t = \nabla \mathbf{v}_i^t$.
3. Similarly, the values μ_i^t , p_i^t at point \mathbf{x}_i^t are obtained by interpolating the fields μ^t , p^t known at time t in the domain $\Omega^s(t)$ using the XFEM approximation.
4. The field variables are updated. Specifically, at point \mathbf{x}_i^{t+dt} , the distribution tensor μ_i^{t+dt} is computed using an explicit Euler time integration scheme according to the evolution equation (3) as

$$\begin{aligned}\boldsymbol{\mu}_i^{t+dt} &= \boldsymbol{\mu}_i^t + \dot{\boldsymbol{\mu}}_i^t dt \\ &= \boldsymbol{\mu}_i^t + \left[k_a \left(\frac{C-c}{c} \right) \mathbf{I} - k_d \boldsymbol{\mu}_i^t + \mathbf{L}_i^t \boldsymbol{\mu}_i^t + \boldsymbol{\mu}_i^t \mathbf{L}_i^t \right] dt\end{aligned}\quad (23)$$

and the pressure p_i^{t+dt} is updated as:

$$p_i^{t+dt} = p_i^t + \dot{p}_i^t dt. \quad (24)$$

These updated values are assigned as the updated regular degrees of freedom $\boldsymbol{\mu}_i^{reg} = \boldsymbol{\mu}_i^{t+dt}$ and $p_i^{reg} = p_i^{t+dt}$.

At this point, we have updated the regular DOF $\boldsymbol{\mu}_i^{reg}$ and p_i^{reg} at each grid node in the domain $\Omega^s(t+dt)$. However, since the interface Γ has moved, the enriched DOF $\boldsymbol{\mu}^{enr}$ and p^{enr} also have to be updated to accurately compute the quantities of $\boldsymbol{\mu}$ and p on the interface. This is done by solving the following equation within the elements cut by Γ

$$\begin{aligned}\boldsymbol{\mu}^{t+dt} - \tilde{\boldsymbol{\mu}} &= \mathbf{0} \quad \forall \mathbf{x} \in \Omega^\Gamma \\ p^{t+dt} - \tilde{p} &= 0 \quad \forall \mathbf{x} \in \Omega^\Gamma\end{aligned}\quad (25)$$

where Ω^Γ is the ensemble of the elements Ω^e that are intersected with Γ . The first terms $\boldsymbol{\mu}^{t+dt}$ and p^{t+dt} are the interpolated values using the nodal DOF. The second terms $\tilde{\boldsymbol{\mu}}$ and \tilde{p} are the updated variables directly computed via Eqs. (23) and (24). The idea here is to find out the enrich DOF such that the interpolated quantities are conformed with the updated values inside the elements that are cut by Γ . The weak form of the above equations read

$$\begin{aligned}(\omega_m, (\boldsymbol{\mu}^{t+dt} - \tilde{\boldsymbol{\mu}}))_{\Omega^\Gamma} &= 0 \\ (\omega_p, (p^{t+dt} - \tilde{p}))_{\Omega^\Gamma} &= 0\end{aligned}\quad (26)$$

and the corresponding discretized forms are given as

$$\begin{aligned}\mathbf{K}_\mu^{enr} \bar{\boldsymbol{\mu}}_g^{enr} &= \mathbf{R}_\mu^{enr}, \\ \mathbf{K}_p^{enr} \bar{p}_g^{enr} &= \mathbf{R}_p^{enr}\end{aligned}\quad (27)$$

where $\bar{\boldsymbol{\mu}}_g^{enr}$ and \bar{p}_g^{enr} are the unknown global vectors of enriched DOF. The detailed expressions of the global tangent matrices, \mathbf{K}_μ^{enr} and \mathbf{K}_p^{enr} , and the residue vectors, \mathbf{R}_μ^{enr} and \mathbf{R}_p^{enr} , are given in the ‘‘Appendix 6’’. In the next sections, we illustrate this numerical approach by considering problems in which the deformation of the dynamic polymer is extreme (i.e. 100% and more). We first start by verifying the method against a closed form solution of uniform material deformation and assess the method’s convergence.

3.5 Benchmark problem: uniaxial tension of a cylinder

To verify and test the performance of the formulation, we first consider a simple problem for which an analytical solution is available. Let us thus consider the stress relaxation of a cylindrical specimen in tension over the course of pseudo time $t = [0, 1]$. The loading history (as shown in Fig. 5a) is summarized as follows: the cylinder is subjected to a tensile deformation along the z direction, as schematically shown in Fig. 3a, until it reaches a final stretch ratio $\lambda = 2$. This stage is followed by a stage in which the cylinder deformation is kept fixed until $t = 1$. In this problem, three networks with attached chain concentrations $c = 1$ are studied. The kinetics of the networks are characterized by the dissociation rates k_d of 0, 1 and 2, respectively. We note here that $k_d = 0$ corresponds to the case that chains do not dissociate and the network is considered to be permanent (or purely elastic).

Analytical solution The first step to obtain the analytical solution is to determine the distribution tensor $\boldsymbol{\mu}$ at time t during the deformation. In this problem, the non-vanishing terms of the velocity gradient tensor \mathbf{L} are $L_{zz}(t) = \dot{\lambda}(t)/\lambda(t)$ and $L_{\rho\rho}(t) = L_{\theta\theta}(t) = -\dot{\lambda}(t)/2\lambda(t)$, where $L_{\theta\theta}$ is the component along the azimuthal direction. Further, since there is no shear deformation, the chain distribution tensor only contains diagonal components denoted by $\mu_{zz}(t)$, $\mu_{\rho\rho}(t)$ and $\mu_{\theta\theta}(t)$, respectively. In the permanent network ($k_d = 0$), it can be found that the distribution tensor only depends on deformation as [74]

$$\mu_{zz}(t) = \lambda(t)^2 \quad \text{and} \quad \mu_{\rho\rho}(t) = \mu_{\theta\theta}(t) = 1/\lambda(t). \quad (28)$$

In the dynamic network, the distribution tensor not only depends on the deformation, but also depends on time due to chain kinetics. Its value at time t is determined by the evolution equation (3) along the longitudinal and lateral direction as

$$\begin{aligned}\dot{\mu}_{zz}(t) &= k_a \frac{C-c}{c} - (k_d - 2L_{zz}(t)) \mu_{zz}(t) \\ \dot{\mu}_{\rho\rho}(t) &= k_a \frac{C-c}{c} - (k_d - 2L_{\rho\rho}(t)) \mu_{\rho\rho}(t)\end{aligned}\quad (29)$$

with their initial values $\mu_{zz}(0) = \mu_{\rho\rho}(0) = 1$. Besides, due to the same magnitude in the velocity gradient, the azimuthal component of the chain distribution tensor $\mu_{\theta\theta}(t)$ is found as the same as the lateral component: $\mu_{\theta\theta}(t) = \mu_{\rho\rho}(t)$. Finally, using the knowledge of the distribution tensor, the longitudinal component of the Cauchy stress tensor $\boldsymbol{\sigma}(t)$ can be computed using the relationship in Eq. (9) as

$$\sigma_{zz}(t) = ck_B T (\mu_{zz}(t) - \mu_{\rho\rho}(t)). \quad (30)$$

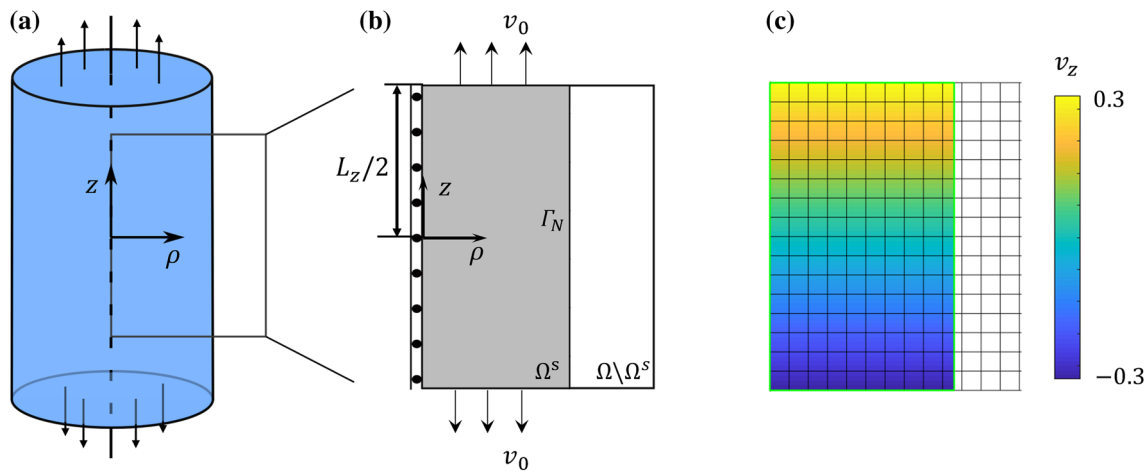


Fig. 3 **a** Schematic of the problem, where a cylinder is been stretched along the vertical direction. **b** Schematic and boundary conditions of the computational domain. **c** The contour of vertical velocity v_z in the computational domain

Numerical solution Here, we model the mechanical response of the cylinder specimen Ω^S in a computational domain of dimension $L_\rho = 1.5R$ and $L_z = 2R$ as shown in Fig. 3b, where R_0 is the initial radius of the cylinder. Extension of the cylinder is modeled by letting materials leave the domain through the top and bottom edges of Ω^S with a constant velocity v_0 . In other words, the boundary conditions are specified in the material domain Ω^S as

$$\begin{cases} \bar{\mathbf{t}} = \mathbf{0} & \text{on } \Gamma_N \\ v_\rho = 0 & \rho = 0 \\ v_z = \pm v_0 & z = \pm L_z/2, t < 1/16 \\ v_z = 0 & z = \pm L_z/2, t > 1/16. \end{cases} \quad (31)$$

In the simulations, the computational domain is discretized with an element size $h = L_\rho/15$ and the time step $\Delta t \propto (h/L_\rho)^2$ is used determined by the Courant-Friedrichs-Lewy (CFL) condition [40]. Here, the time step is chosen as $\Delta t = 1/240$.

Result We first test the numerical scheme using the LBB condition described in Sect. 3.2 for both elastic network ($k_d = 0$) and dynamic network ($k_d = 2$). For this, we considered six successive mesh refinements and compute the corresponding inf-sup values as shown in Fig. 4. For both networks, the inf-sup value does not drop to zero, indicating that the LBB condition is passed.

Figure 5a shows the vertical stretch ratio $\lambda(t)$ of the cylinder as a function of time while Fig. 5b depicts the numerical results for the normalized vertical stress $\sigma_{zz}^*(t) = \sigma_{zz}(t)/ck_B T$ corresponding to $k_d = 0, 1$ and 2 , respectively. The effect of chain kinetics is quite apparent: the stress in the permanent network remains constant after the deformation is fixed, while the stress in dynamic networks relaxes towards

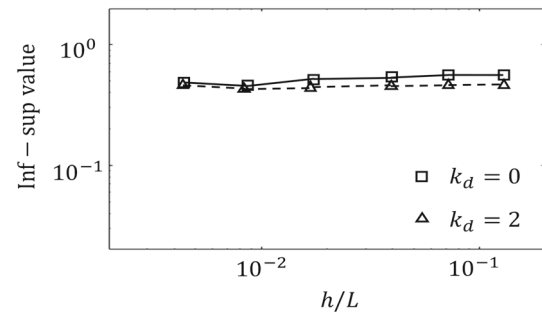


Fig. 4 Inf-sup parameter as a function of meshsize

$\sigma_{zz}^* = 0$ with a higher rate when k_d increases. In addition to the numerical results, analytical solutions for σ_{zz}^* are also obtained for each network and were plotted with symbols in Fig. 3b, where good agreements are obtained for all three dissociation rates.

In order to assess the performance of the formulation, we further investigated the convergence of error made in calculating the stress σ_{zz}^* for the networks with $k_d = 0$ and 2 as functions of both relative meshsize h/L_ρ and timestep Δt . The L^2 -norm error e in stress is calculated as

$$e = \left[(\sigma_{zz}^{*n} - \sigma_{zz}^{*a})^2 \right]^{\frac{1}{2}} \quad (32)$$

where σ_{zz}^{*a} stands for the analytical solution obtained from Eq. (30). The rates of convergence p are evaluated by performing the power law fitting of the error with respect to h/L_ρ and Δt . The fitting function reads as

$$e^{fit} = k_1(\Delta x)^p$$

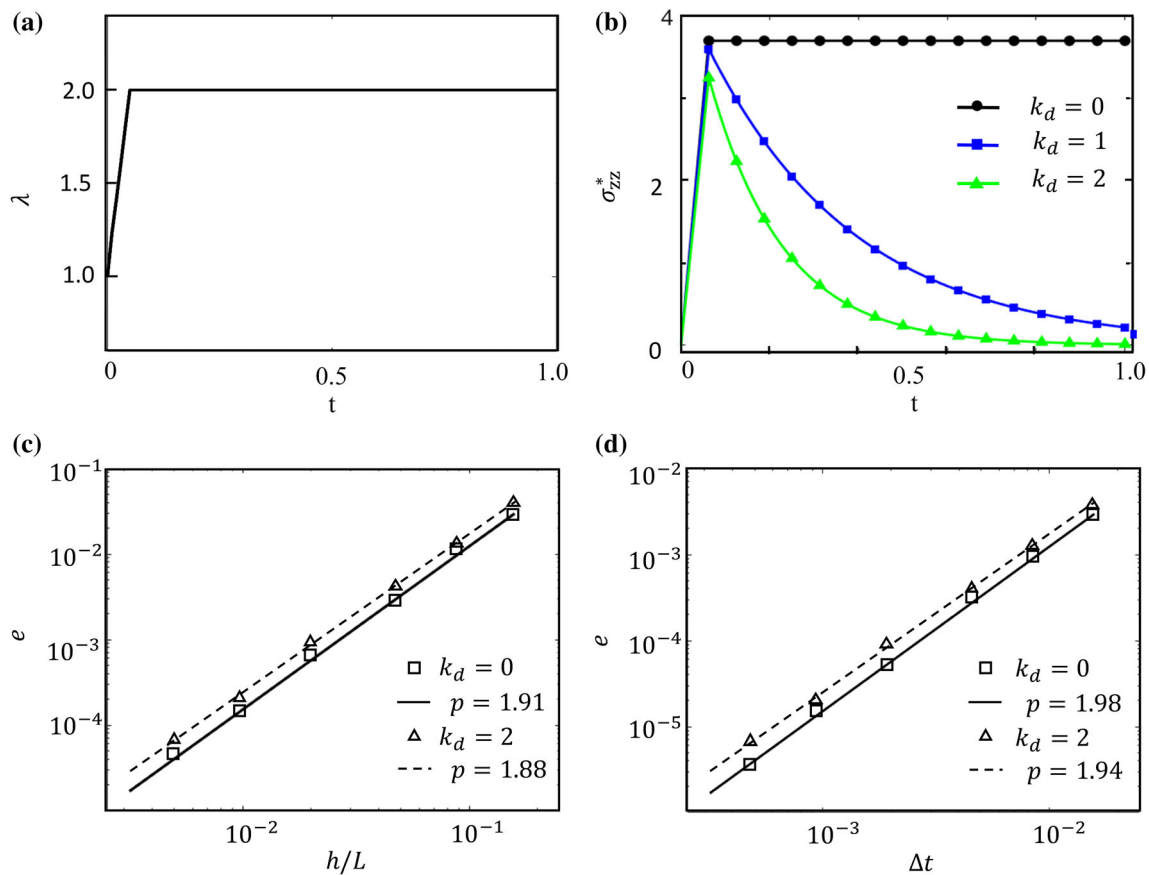


Fig. 5 **a** The applied deformation of the cylinder during relaxation, where it is fastly stretched until $\lambda = 2$. **b** The evolution of stress component σ_{zz} for polymer networks of $k_d = 0, 1$ and 2 , where stress relaxation is observed for dynamic network. The numerical results (lines) have

good agreement with analytical solutions (symbols). **c** Convergence of the errors to the relative meshsize h/L , the errors converge to zero as $O(h^{1.91})$. **d** Convergence of the errors to the timestep Δt , the errors converge to zero as $O(\Delta t^{1.98})$

where k_1 is a fitting constant and Δx is the discretization parameter (corresponding to h/L_ρ or Δt in this problem). Results presented in Fig. 5 show rates of convergence at the orders of $O((h/L_\rho)^{1.9})$ and $O(\Delta t^2)$, which agree well with results reported in [26] for the PMIM algorithm showing the convergence rate around $O(h^2)$ and the convergence rate of the explicit Euler time integration scheme [5]. To further estimate the efficiency of this formulation. We measure the time necessary to complete one time step. We find this time to be about 2.7 s, which is acceptable and practical to study a variety of 2D and axisymmetric problems. This cost can be further broken down into the cost of the three main formulation steps (discussed in Sects. 3.1, 3.3 and 3.4, respectively) by their relative percentage: (1) XFEM solution: 48%; (2) tracking the evolution of the interface: 6% and (3) Lagrangian transport of μ and p : 46%. In general, we expect that this cost is roughly proportional to the number of element used to discretize the domain. Some variations are also expected from problem to problem due to the differences in geometry and loading condition.

4 Rheology of dynamic networks

In this section, we aim to investigate the behavior of dynamic polymer networks undergoing large deformations. Three different examples are considered: the first is the growth of a spherical cavity under pressure within the polymer network; the second explores the indentation of a polymer sphere under large deformation; the last problem finally considers the sinking of a heavy ball in a cylindrical polymer specimen. All problems are solved within axisymmetric assumptions.

4.1 Cavitation rheology

In the first problem, we investigate the mechanics of Cavitation Rheology (CR) of dynamic polymers. CR is a technique that allows one to determine the local modulus of a point within a soft material [81,82]. This method involves growing a cavity inside the material using a syringe needle (Fig. 6a) and measuring the critical applied pressure P at which material instability is observed. For example, for elastomers,

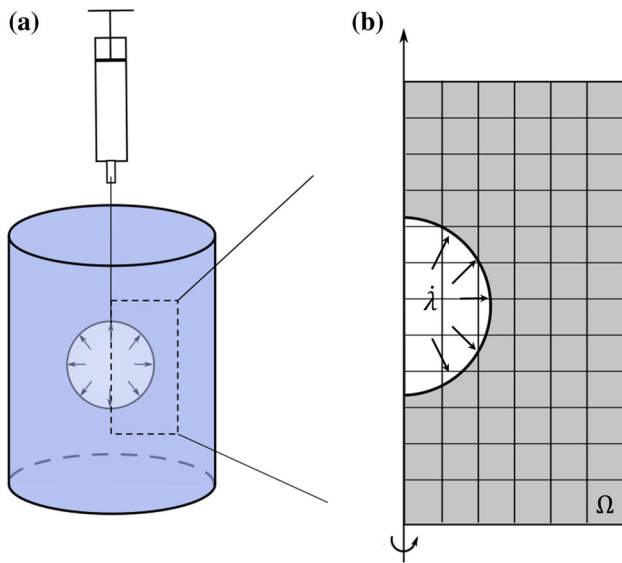


Fig. 6 **a** Schematic of CR of a cylindrical polymer. **b** The schematic of the computational domain. In the numerical simulation, the growth of the cavity is controlled by $\dot{\lambda} = \dot{R}/R_0$

one can relate the normalized applied pressure $P^* = P/E$ (where E is the Young's modulus of material) to the change in the radius of the cavity $\lambda = R/R_0$ as [30,79]

$$P^* = \frac{5}{6} - \frac{2}{3\lambda} - \frac{1}{6\lambda^4}. \quad (33)$$

From the above equation, we can see that P^* asymptotes to a constant $5/6$ as λ increases. Therefore, when P^* is greater than $5/6$, the cavity would expand without bond.

In the numerical simulation, we consider a circular cavity of initial radius R_0 , delimited by its interface Γ , located on the rotational axis of the computational domain Ω^s , as shown

in Fig. 6b. To avoid boundary effects, the height and width of the computational domain are set as $L_z = 8R_0$ and $L_\rho = 16R_0$ and stress-free conditions are applied on the boundaries except for the rotational axis. To avoid singularities in the solution, we adopted velocity controlled boundary conditions such that the growth of the cavity is driven by a constant rate of increase in its radius $\dot{\lambda} = \dot{R}/R_0$. The pressure P^* is then found from the force balance of the material points on the interface [79]: $P^* = -\sigma_{rr}^*$ on Γ , where $\sigma_{rr}^* = \sigma_{rr}/E$ is the normalized stress along the radial direction of the cavity. Body forces are neglected in this problem to be consistent with the analytical study [30].

Permanent network In Fig. 7a, we show four zoom-in snapshots of the cavity as it grows from $\lambda = 1$ to 4 and the stress field σ_{rr} for the permanent network ($k_d = 0$). In Fig. 7b, we show the change in P^* as a function of λ . Numerical predictions are plotted by the solid lines and analytical results from Eq. (33) are depicted by black squares, where good agreement is achieved even for large deformation ($\lambda = 4$).

Dynamic network When the network is dynamic, the kinetics of chain dissociation and associations can play a significant role in the cavity expansion. In this case, the pressure in a steadily expanding cavity (i.e., constant $\dot{\lambda}$) results from two competing mechanisms: the stretch of chains, leading to an increase in pressure and the dissociation and re-association of the chains that tend to reduce pressure. We note that the rate of radial deformation L_{rr} is computed as $L_{rr} = \dot{R}/R = \dot{\lambda}/\lambda$. Since the chain stretch follows the macroscopic deformation, the strain rate of the chains is large when λ is small while it decreases monotonically as λ increases. Therefore, chain kinetics plays an increasingly important role in determining the pressure P^* as λ increases.

In Fig. 8a, we show the change in pressure for networks with different chain kinetics, characterized by the normalized

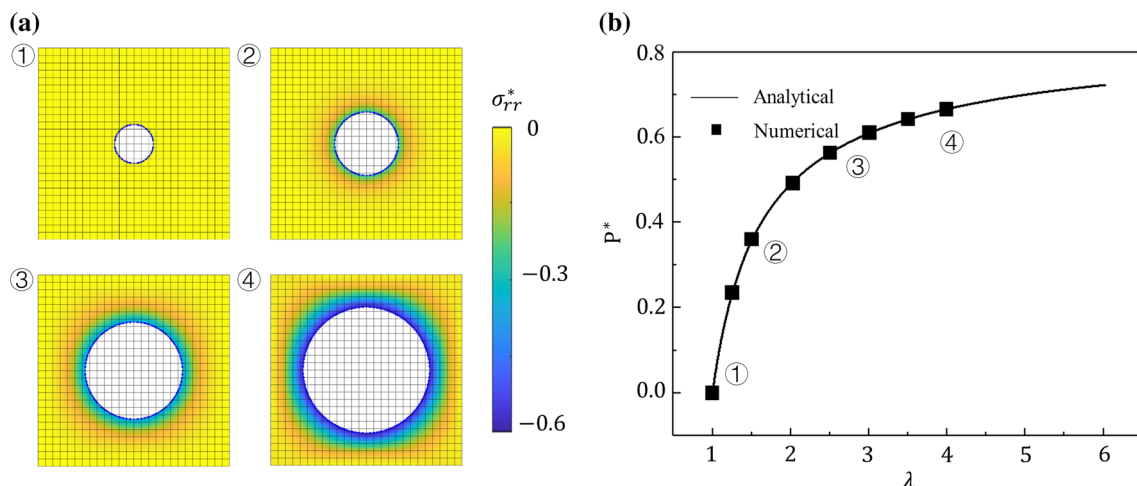


Fig. 7 **a** Four snapshots of the growth of cavity and the evolution of stress σ_{rr} along the radial direction. **b** The change in pressure to expand the cavity as a function of λ and the comparison between numerical and analytical solutions

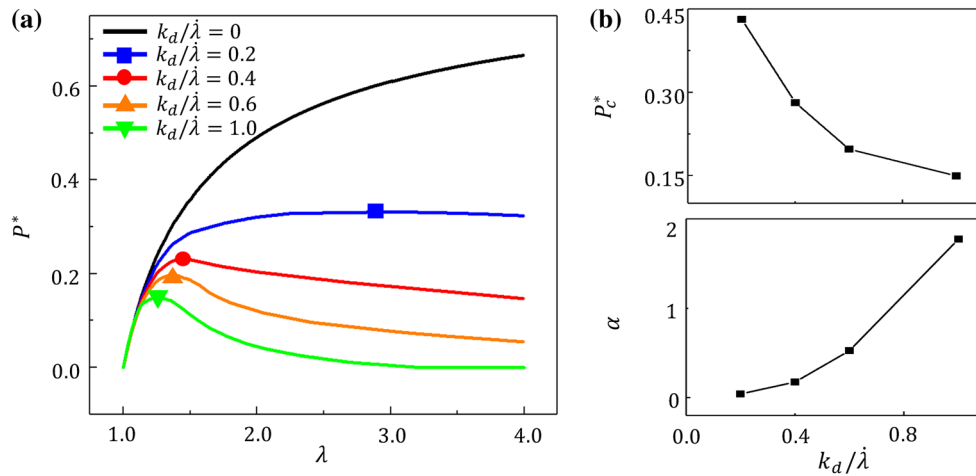


Fig. 8 **a** $P/E - \lambda$ relation predicted by numerical model for different chain dynamics. For dynamic chains, their maximum pressure P_c during cavity growth is pointed by the symbol. **b** Summary of the maximum pressure P_c and the decreasing rate of the dynamic networks

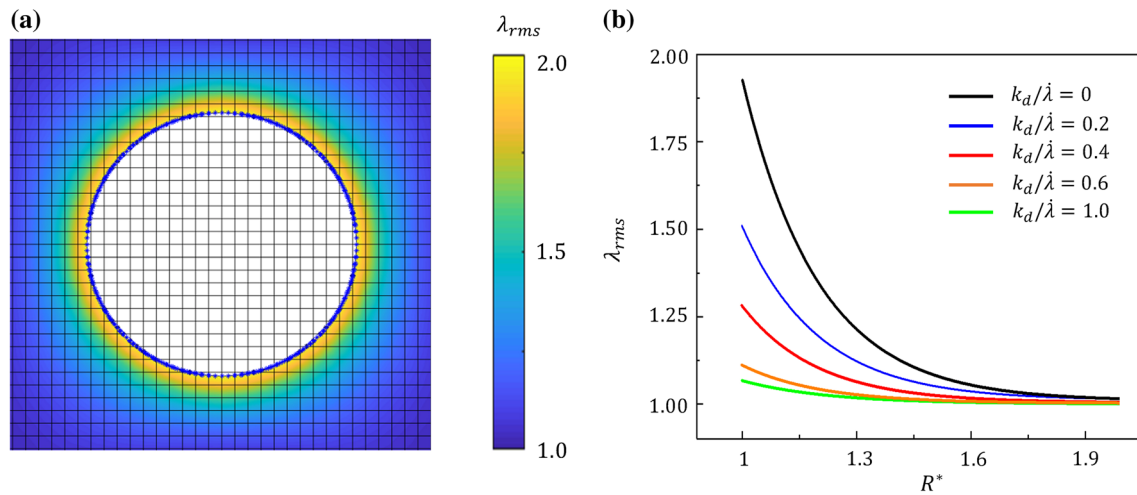


Fig. 9 **a** Root mean square of chain stretch λ_{rms} for the permanent network when deformation $\lambda = 4$. **b** The magnitude of λ_{rms} as a function of the distance from the cavity center

rates $k_d/\dot{\lambda}$. As expected, the pressure P^* first increases with λ since the strain rate of the chains is high. However, after a maximal pressure P_c^* (marked by symbols) is reached, chain dissociation and re-association becomes the dominating factor and P^* decreases monotonically as the cavity expands. This result indicates that, for CR experiments that are usually controlled by pressure, the kinetics of the chains can actually change the critical pressure when material instability occurs. To further relate this change in pressure to the chain kinetics, we use the following equation to fit the decreasing segment of each curve

$$\frac{P}{E} = \frac{P_c}{E} e^{-\alpha(\lambda - \lambda_c)}. \quad (34)$$

Fig. 8b plots the critical pressure P_c and the decreasing rate α as functions of $k_d/\dot{\lambda}$. It is shown that P_c^* decreases signif-

icantly as $k_d/\dot{\lambda}$ increases. Simulations finally show that, as expected, networks with faster kinetics $k_d/\dot{\lambda}$ display a higher decreasing rate.

Stretch of chains In addition to measuring the pressure, the effect of chain kinetics can also be understood through the physical states of the network. For example, in Fig. 9a, we show the root mean square of chain stretch λ_{rms} (computed by Eq. (11)) in the area around the interface for $k_d/\dot{\lambda} = 0$. In Fig. 9b, we also show λ_{rms} as a function of the normalized distance $R^* = d/R$, where d is the distance of a material point from the center of the cavity. We observe here that chains are stretched in the neighborhood of the interface (i.e., $R^* < 1.3$), while those in the far field (i.e., $R^* = 1.9$) remain unstretched. By comparing the plots of different chain kinetics $k_d/\dot{\lambda}$, one sees that chain stretch decreases significantly as $k_d/\dot{\lambda}$ increases, since the ability of chains to detach and

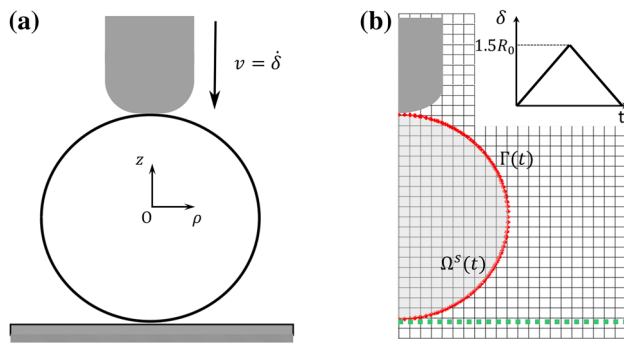


Fig. 10 **a** Schematic of indentation, the indenter moves at a constant velocity $\dot{\delta}$. **b** Numerical domain and the indenting depth δ as a function of time

reattach relaxes results in an overall drop in their average strain.

4.2 Indentation of specimens made of dynamic polymers

Indentation is a widely used technique to measure the mechanical properties of the material, such as the Young's modulus [69]. For soft materials such as polymers or bio-tissues that exhibit transient behaviors, visco-elastic properties can be characterized by different types of indentation tests, including the cyclic indentation [44], creep [55] or relaxation [37]. Since the shapes of materials may be significantly changed during these tests, modeling these problems with Lagrangian formulation is challenging and the amount of deformation is limited. In this section, we consider two indentation tests of dynamic polymer networks: we will first consider the cyclic indentation of a spherical polymer body, and then the indentation creep of a cylindrical polymer is investigated.

4.2.1 Cyclic indentation of a polymer sphere

Let us consider a polymer sphere of radius R_0 that is placed on a flat substrate and indented by a rigid indenter on the top surface, as shown in Fig. 10a, where the bottom part of the indenter is spherical with its radius $R_I = 0.6R_0$. The deformation is applied in a symmetric manner, where the indenter is first moved downwards with a constant rate $\dot{\delta}$ until a maximum depth $\delta = 1.5R_0$ is reached. Immediately after, the indenter is moved upwards with the same rate until it goes back to the initial position (see the $\delta - t$ curve in the subplot of Fig. 10b).

The contact between the polymer and the rigid solids (indenter and substrate) is modeled here by an artificial repulsive traction $\bar{\mathbf{t}}$ applied on the portion of the interface Γ . This repulsion force is defined to prevent penetration between the

polymer and the solids. For a point \mathbf{x} on the interface Γ , the repulsive traction is computed as

$$\bar{\mathbf{t}}(\mathbf{x}) = \begin{cases} k_{rep}(d_0 - d)/d_0 \bar{\mathbf{n}} & \text{if } d < d_0 \\ \mathbf{0} & \text{if } d > d_0 \end{cases} \quad (35)$$

where $k_{rep} = \exp(d_0 - d)$ is the repulsion coefficient; d is the closest distance between \mathbf{x} and the rigid solids and d_0 is a cut-off distance, below which the repulsive force is activated. In order to mimic the contact, d_0 is taken as a very small value ($R_0/40$). The deformation of the polymer is characterized by the relative depth of indentation δ/R_0 , while the mechanical response is quantified by the total repulsion force $F = \int_{\Omega_a} \bar{\mathbf{t}} \cdot \hat{\mathbf{e}}_z d\Omega_a$ between the substrate and the polymer, where $\hat{\mathbf{e}}_z$ is the normal vector along the vertical direction and Ω_a is the area of the polymer body that is considered to be in contact with the substrate.

Analytical solution When the deformation is small, the force between the indenter and the sphere can be analytically obtained by the Hertz theory. In this theory, the contact force F on a linear elastic sphere, characterized by the Young's modulus E , and a rigid sphere can be computed as a function of indentation depth δ as

$$F = \frac{4E}{3(1 - \nu^2)} R^{1/2} \delta^{3/2} \quad (36)$$

where ν is the Poisson's ratio of the material and R is the effective radius computed by $1/R = 1/R_1 + 1/R_2$, with R_1 and R_2 are the respective radii of the contacted spheres. In our problem, the Young's modulus is related to the attached chain density by $E = 3ck_B T$, ν is taken as 0.5 for incompressibility and the effective radius R has the value $R = 3R_0/8$ according to R_I and R_0 . Using these variables, the force between the indenter and the polymer sphere can be found from Eq. (36) as

$$F = \frac{8ck_B T}{3} \left(\frac{3}{2} R_0 \right)^{\frac{1}{2}} \delta^{\frac{3}{2}}. \quad (37)$$

For the permanent network $k_d = 0$, we compared the numerical prediction of the loading curve to the one that is predicted by Eq. (37) in the regime $\delta < R_I$. At small δ/R , good agreements are obtained between the numerical and the analytical solution, as shown in the subplot. However, since the Hertz theory assumes linear elasticity, its prediction deviates from the numerics when δ becomes larger.

Additionally, in Fig. 11a, we also show the force-displacement curve predicted by the model for two dynamic polymer networks, characterized by the normalized rate $k_d/\dot{\delta} = 0, 1$ and 2. Our results show that due to the effect of chain kinetics, the force required to indent the dynamic polymer is smaller compared to the permanent network

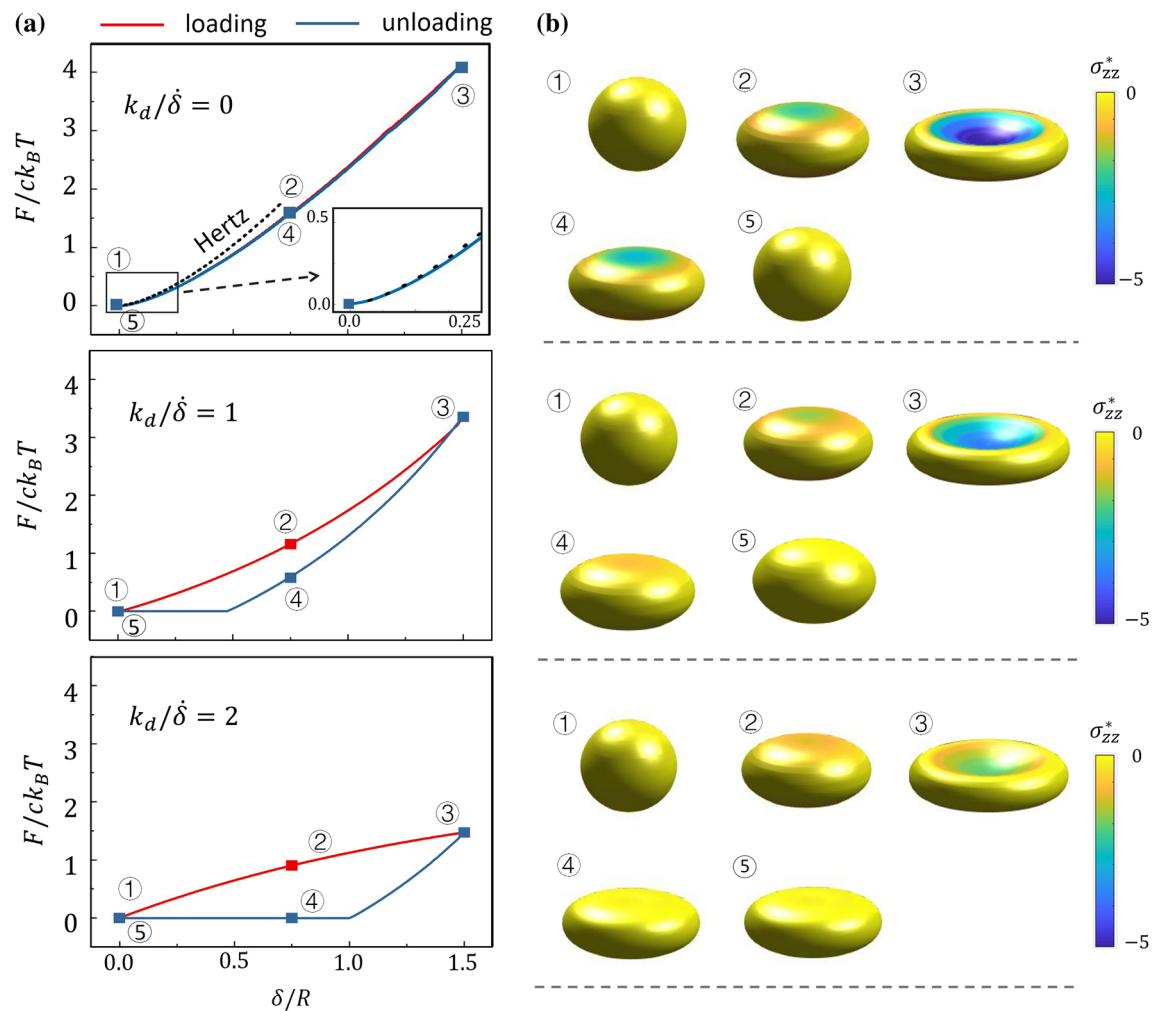


Fig. 11 **a** Force-displacement relationship for different networks over the course of one loading-unloading cycle. **b** Evolution of the shapes and the stress σ_{zz} of the polymer

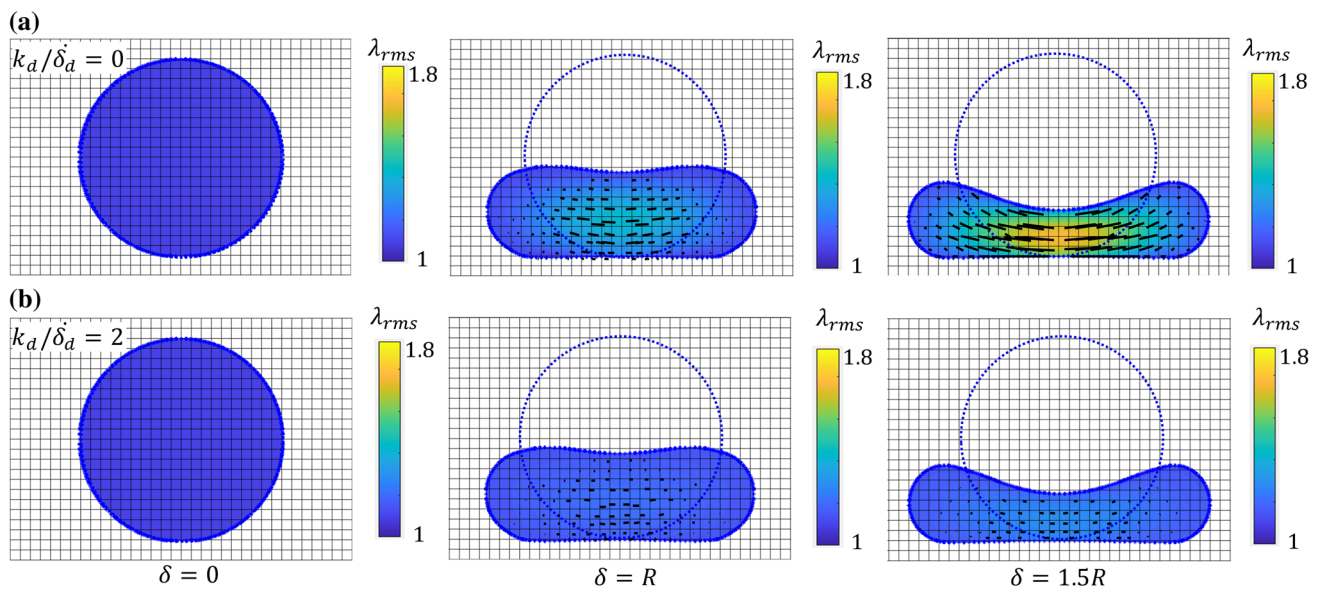


Fig. 12 **a** Evolution of root mean square of chain stretch λ_{rms} of (a) permanent network and **b** dynamic network during the loading stage

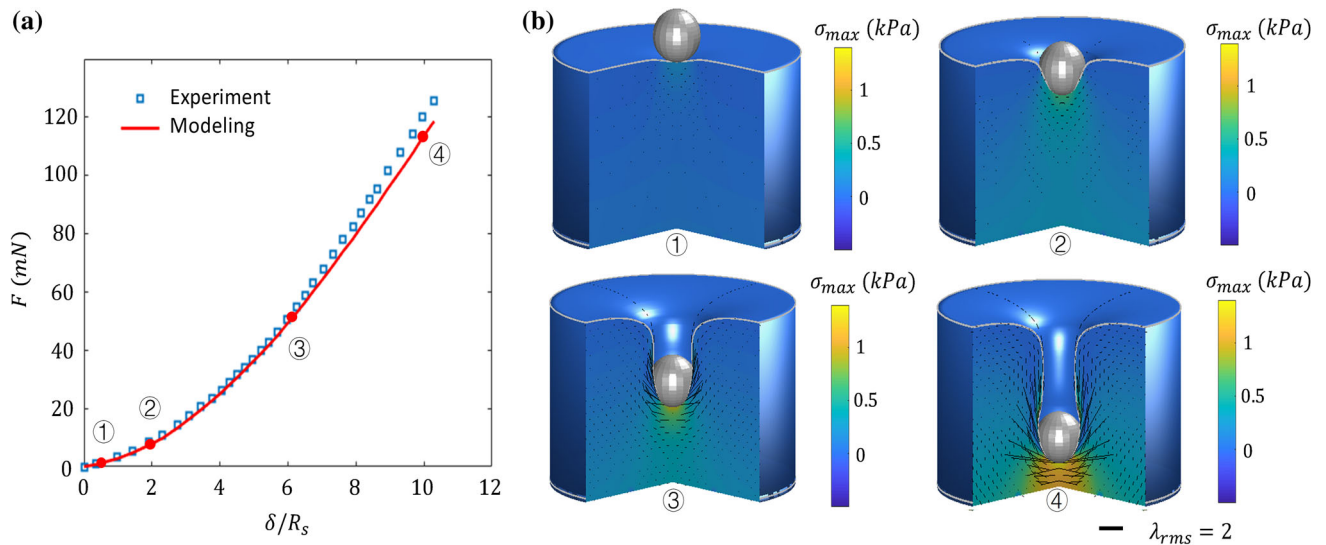


Fig. 13 **a** The comparison of force-displacement curve for between experiment and modeling results. **b** Four Snapshots of indentation for the network. We use black lines to depict the chain elongations $\lambda_{rms} - 1$ (scale bar equals $\lambda_{rms} - 1 = 1$) and the contour plot to show the maximum principle stress

($k_d/\dot{\delta} = 0$). Besides, the loading and unloading curve for the permanent network overlap while significant hysteresis is observed for dynamic networks. Recalling that the area of the hysteresis loop represents the dissipation of energy in one cycle, we can see the energy dissipation increases monotonically with $k_d/\dot{\delta}$ due to the higher rates of chain dissociation and re-association. In Fig. 11b, we show the normalized vertical stress $\sigma_{zz}^* = \sigma_{zz}/ck_B T$ and the shape of the polymer at 5 different time steps during the deformation cycle. As a result of energy dissipation, the stress in the network is smaller for larger $k_d/\dot{\delta}$, and permanent deformations are observed at the end of the cycle.

To further investigate the effect of chain kinetics on the network, Fig. 12a depicts the evolution of average chain stretch λ_{rms} in contour plots during the loading stage for the permanent network and the dynamic network with $k_d/\dot{\delta} = 2$. In addition to the contour plots, the stretch of the chains is also visualized using black lines, which are aligned with the maximum stretch direction (principle direction of the distribution tensor μ) and whose lengths represent the chain elongations $\lambda_{rms} - 1$. It is shown that the chains are stretched laterally during the indentation due to the incompressibility. Compared to the permanent network, λ_{rms} is significantly smaller for $k_d/\dot{\delta} = 2$, which, in a physical sense, explains the decrease in stress and the dissipation of energy as shown in Fig. 11.

4.2.2 Deep Indentation of a cylinder

In the previous two examples, although the polymer undergoes large deformation, its shape remains uniform. Herein, to illustrate the advantages of the CEL formulation, we investigate the deep indentation of a cylindrical polymer which

exhibits extreme deformation. We consider two cases: (a) the indentation of a purely elastic gel for which our results are compared with experimental data and (b) the indentation of a dynamic polymer by a heavy sphere. The deep indentation of a purely elastic cylindrical hydrogel by a spherical glass bead is first considered for comparison purposes with the experimental study of Fakhouri et al. [22]. To simulate this test and compare the predicted loading-displacement curve with the data reported, we consider a cylindrical domain with radius $R_0 = 10$ mm whose lateral expansion is constrained (Fig. 13). A rigid sphere with radius $R_s = 0.65$ mm is then placed on the top surface of the cylinder and moved downward at constant velocity $v = 0.1$ mm/s. As in previous examples, the contact between the sphere and the hydrogel is modeled by an artificial repulsive force and the mechanical response is quantified by the total repulsion F . To model the purely elastic network, the rate of dissociation and re-association, k_d and k_a , are set to be zero. Since there is no reported elastic modulus of the hydrogel used for this experiment, we consider the Young's Modulus $E = 3ck_B T$ as a fitting parameter for the numerical model. Figure 13a shows the experimental data extracted from ESI Fig. S3 in [22], as well as the result of the numerical simulations. The Young's modulus used in the numerical simulation is $E = 2.3$ kPa, which is within the range of modulus reported in [22] for the hydrogel. It is shown that the modeling result matches well with experimental measurements up to the indentation depth of $\delta = 5R_s$. When $\delta > 5R_s$, the force reported in experiment becomes higher, suggesting that the material exhibits strain hardening. It is known that the strain-hardening of polymers at large strain arises from the nonlinear mechanical response of the chains $|f|$ as their end-to-end distance approaches the

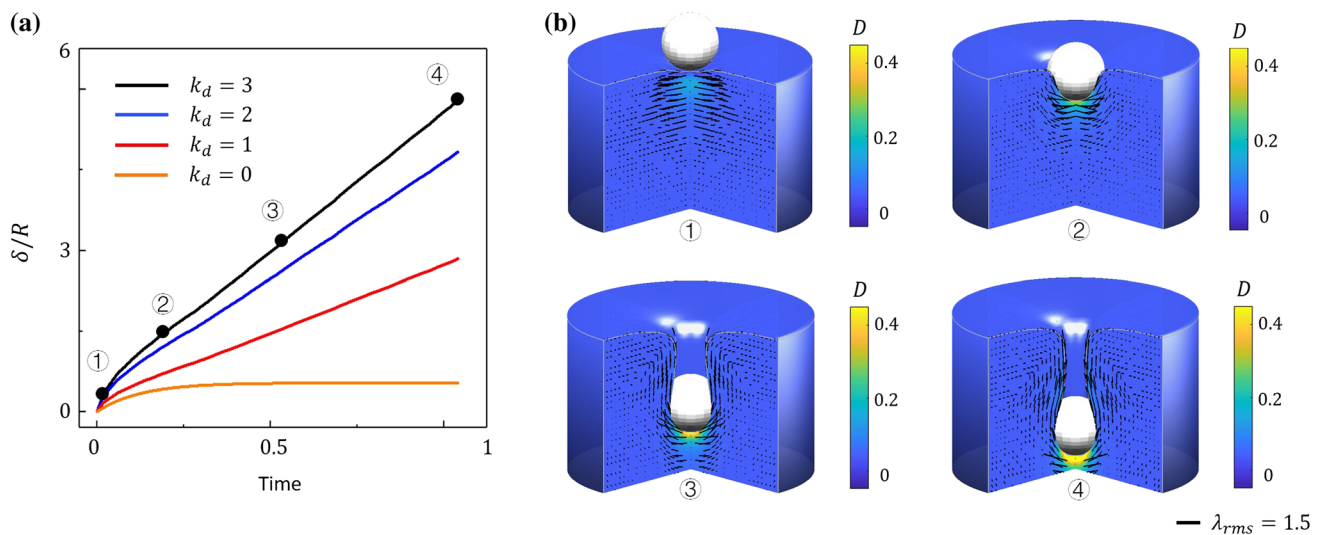


Fig. 14 **a** The indentation depth of the rigid ball in time for different networks. **b** Snapshots of indentation for the network $k_d/\dot{\lambda} = 3$. The scale bar equals $\lambda_{rms} - 1 = 0.5$

contour length [17], a phenomenon that is beyond the scope of this study. The strain-hardening effect can however be considered within the proposed model by using a Langevin chain model [68,70]. Figure 13b shows four zoom-in snapshots of the deformation of the hydrogel in the neighborhood of the sphere. Again, we use black lines to depict the magnitude and the elongation of chains $\lambda_{rms} - 1$. It is shown that the magnitude of elongation increases as the sphere moves down in the cylinder, and the maximal elongation is observed in the area under the indentation region. In the contour plot, we show the maximum principle stress in the material, where we can see that the stress is the highest in the area that the chains are mostly elongated.

In the second example, we consider a dynamic network ($k_d = k_a > 0$) that deforms under the action of a (sinking) heavy spherical indenter placed on its surface. For this, the density of the sphere ρ_s is taken as 1.5 times the density ρ_0 of the polymer and the radius of the sphere is R_s is 0.25 time of the radius R_0 of the cylindrical specimen. Considering the effect of gravitational force, the rigid ball sinks in time and indents the cylinder. In this problem, the deformation of networks with four different kinetics are considered, including a permanent network ($k_d = 0 \text{ s}^{-1}$) and three dynamic networks characterized by the rates $k_d = 1, 2$, and 3 s^{-1} . The body force in these networks is accounted as $\mathbf{b} = \rho_0 \mathbf{g}$, where \mathbf{g} is the gravitational acceleration.

In this problem, the cylinder undergoes a constant load given by the gravitational force of the rigid ball $F = \rho_s V \mathbf{g}$, where $V = 4\pi R_s^3/3$ is the volume of the rigid ball. In Fig. 14a, we show the depths of indentation normalized by the radius of the ball δ/R . The rigid ball in the permanent network remains static after reaching an equilibrium depth. In contrast, we clearly see the typical primary stages and

the secondary stage, a.k.a. the steady state, of creep behavior for the dynamic networks [19]. It can further be seen that, as expected, the indentation rate $\dot{\delta}$ increase with k_d . In Fig. 14b, snapshots about the evolution of the network with $k_d = 3$ during the creep, where the contour plots show the energy dissipations D and black lines are used to visualize the average chain elongations. We observe that the maximal dissipation is found within the same area where the chains are most stretched (right underneath the rigid ball), since chains dissociate in a highly stretched states. Besides, although the polymer undergoes extreme deformation from ① to ④, the average chain elongation observed in the network does not significantly change due to the dissociation and re-association of chains.

From the numerical perspective, the cylinder is extremely distorted during the creep and the interface possess a high curvature in the configuration shown in Fig. 14b④. The conventional Lagrangian formulation would suffer from large mesh distortion even with extensive remeshing, while the CEL formulation remains stable through the deformation history. We note here that when high curvatures appear, the method may benefit from local mesh refinement, which is straightforward for the type regular mesh required for this methodology [73].

5 Conclusion

In summary, we introduced a coupled Eulerian–Lagrangian (CEL) formulation to model the large deformation of dynamic polymer networks. The equilibrium equations are solved in an Eulerian framework and the transport equations for chain distribution tensor $\boldsymbol{\mu}$ and pressure p are solved in

an updated Lagrangian framework. The numerical results of different examples indicate the validity of the framework, as well as the microscopic chain dissociation and association kinetics in the dynamic networks in different problems. This framework is especially advantageous when deformation is large or even extreme, which is widely observed in soft materials, including soft polymers [63] and biological tissues [45] or soft colloids squeezing through pores [6,27]. We note here that our methodology requires smooth solid boundaries; the extension to sharp corners has however been considered with XFEM [28] and may be considered as a solution in the future. Future work can also consider the binding and self-healing of polymer interface [27,53], as well as more complicated behavior of materials, arising from the entanglement of chains [15,16] and the plastic yielding of materials [76]. Overall, this framework provides an attractive avenue to study the mechanics of the new class of polymers that possess reversible bonds [38,77] and potentially contribute to the computational design of material for self-healing [32], active materials [42,48], tissue engineering scaffolds [1,61] but will also contribute to a better understanding of biological cells [23,71,72].

Acknowledgements The author acknowledges the support of the National Science Foundation under the NSF CAREER award 1350090. Research reported in this publication was also partially supported by the National Institute of Arthritis and Musculoskeletal and Skin Diseases of the National Institutes of Health under Award Number 1R01AR065441. The content is solely the responsibility of the authors and does not necessarily represent the official views of the National Institutes of Health.

Appendix 1: rate of change in stored elastic energy

To derive the rate of change in elastic energy, we first rewrite Eq. (7) as

$$\Delta\Psi = \Psi - \Psi_0 + p \left(\frac{C}{C_0} - 1 \right)$$

where $\Psi = \frac{ck_B T}{2} \text{tr}(\boldsymbol{\mu})$ and $\Psi_0 = \frac{ck_B T}{2} \text{tr}(\boldsymbol{\mu}_0)$ are the stored elastic energy at the current and the stress-free state, respectively. Note that for bond exchange reaction, the change of chain concentration is only caused by the change in volume. Therefore, the third term on the right hand side can be equivalently written in terms of volume as $p(\frac{V}{V_0} - 1)$. The rate of change in the stored elastic energy is then written as

$$\Delta\dot{\Psi} = \dot{\Psi} - \dot{\Psi}_0 + p \text{tr}(\mathbf{L}) \quad (38)$$

where $\text{tr}(\mathbf{L}) = \mathbf{I} : \mathbf{L}$ is the rate of change in volume. We first evaluate the term corresponding to the current state

$$\dot{\Psi} = \frac{ck_B T}{2} \dot{\boldsymbol{\mu}} : \mathbf{I}. \quad (39)$$

We then employ the evolution equation (Eq. (4)) and the above equation becomes

$$\dot{\Psi} = \frac{ck_B T}{2} (2\boldsymbol{\mu} : \mathbf{L}) - k_d \frac{ck_B T}{2} (\boldsymbol{\mu} - \boldsymbol{\mu}_0). \quad (40)$$

Similarly, the term corresponding to the stress-free configuration in Eq. (38) can be obtained as

$$\dot{\Psi}_0 = \frac{ck_B T}{2} (2\boldsymbol{\mu}_0 : \mathbf{L}) - k_d \frac{ck_B T}{2} (\boldsymbol{\mu}_0 - \boldsymbol{\mu}_0). \quad (41)$$

Combining Eqs. (38), (40) and (41), the rate of change in stored elastic energy reads

$$\Delta\dot{\Psi}_e = [ck_B T(\boldsymbol{\mu} - \boldsymbol{\mu}_0) + p\mathbf{I}] : \mathbf{L} - k_d \frac{ck_B T}{2} \text{tr}(\boldsymbol{\mu} - \boldsymbol{\mu}_0). \quad (42)$$

Appendix 2: field equations in cylindrical coordinates

In cylindrical coordinates, the balance of momentum equation can be written along the radial and the longitudinal direction as

$$\begin{aligned} \frac{\partial \dot{\sigma}_{\rho\rho}}{\partial \rho} + \frac{1}{r}(\dot{\sigma}_{\rho\rho} - \sigma_{\theta\theta}) + \frac{\partial \dot{P}}{\partial \rho} &= 0 \\ \frac{\partial \dot{\sigma}_{\rho z}}{\partial \rho} + \frac{\partial \dot{\sigma}_{zz}}{\partial z} + \frac{1}{\rho} \dot{\sigma}_{\rho z} + \frac{\partial \dot{P}}{\partial z} &= 0. \end{aligned}$$

The condition of incompressibility reads

$$\frac{1}{\rho} \frac{\partial}{\partial \rho}(\rho v_\rho) + \frac{\partial v_z}{\partial z} = 0.$$

Appendix 3: discretization of element degrees of freedoms

In the numerical study, XFEM is implemented in the element shape functions to account for the discontinuities. For split elements, the shape function matrices \mathbf{N}_v , \mathbf{N}_μ , \mathbf{N}_p and the vectors of element nodal values \mathbf{v}^e , $\boldsymbol{\mu}^e$, \mathbf{p}^e contain both standard and enriched DOFs and are defined as

$$\text{nodal DOFs} \begin{cases} \mathbf{v}^e = [\tilde{\mathbf{v}}^{reg}; \tilde{\mathbf{v}}^{enr}]_{36 \times 1}, \\ \tilde{\mathbf{v}}^{reg} = [v_\rho^1, v_z^1 \dots v_\rho^9, v_z^9]^T_{18 \times r}, \\ \tilde{\mathbf{v}}^{enr} = [\hat{v}_\rho^1, \hat{v}_z^1 \dots \hat{v}_\rho^9, \hat{v}_z^9]^T_{18 \times 1}; \\ \boldsymbol{\mu}^e = [\tilde{\boldsymbol{\mu}}^{reg}; \tilde{\boldsymbol{\mu}}^{enr}]_{40 \times 1}, \\ \dot{\mathbf{p}}^e = [\tilde{\mathbf{p}}^{reg}; \tilde{\mathbf{p}}^{enr}]_{8 \times 1}, \\ \tilde{\mathbf{p}}^{reg} = [\dot{p}^1, \dots, \dot{p}^4]^T_{4 \times r}, \\ \tilde{\mathbf{p}}^{enr} = [\hat{p}^1, \dots, \hat{p}^4]^T_{4 \times 1}; \end{cases}$$

$$\text{shape functions} \begin{cases} \mathbf{N}_v = [\mathbf{N}_v^{reg}; \mathbf{N}_v^{enr}]_{2 \times 36}, \\ \mathbf{N}_p = [\mathbf{N}_p^{reg}; \mathbf{N}_p^{enr}]_{1 \times 8}, \end{cases}$$

where

$$\begin{aligned} \mathbf{N}_v^{reg} &= [\mathbf{N}_v^1, \dots, \mathbf{N}_v^9]_{2 \times 18}, \\ \mathbf{N}_v^{enr} &= [\mathcal{S}^1 \mathbf{N}_v^1, \dots, \mathcal{S}^9 \mathbf{N}_v^9]_{2 \times 18} \end{aligned} \quad (43)$$

$$\begin{aligned} \mathbf{N}_p^{reg} &= [N_4^1, \dots, N_4^4]_{1 \times 4}, \\ \mathbf{N}_p^{enr} &= [\mathcal{S}^1 N_4^1, \dots, \mathcal{S}^4 N_4^4]_{1 \times 4} \end{aligned} \quad (44)$$

$$\text{and } \mathbf{N}_v^I = \begin{bmatrix} N_9^I & 0 \\ 0 & N_9^I \end{bmatrix}.$$

Here, we note that $\mathcal{S}^I = H(\phi(\mathbf{x}) - H(\phi(\mathbf{x}^I)))$. To compute the deformation rate of the material, velocity gradient tensor and the divergence of velocity are written as

$$\mathbf{D} = (\nabla \mathbf{v})^s = \mathbf{B}_v \cdot \mathbf{v}^e \quad \text{and} \quad \nabla \cdot \mathbf{v} = \hat{\mathbf{B}}_v \cdot \mathbf{v}^e.$$

The rate \mathbf{B}_v and $\hat{\mathbf{B}}_v$ matrices that are related to the nodal velocities to deformation rates are written in the cylindrical coordinates as

$$\mathbf{B}_v = [\mathbf{B}_v^1, \dots, \mathbf{B}_v^9, \mathcal{S}^1 \mathbf{B}_v^1, \dots, \mathcal{S}^9 \mathbf{B}_v^9]_{4 \times 36}$$

$$\text{with } \mathbf{B}_v^I = \begin{bmatrix} \frac{\partial N_9^I}{\partial \rho} & 0 \\ 0 & \frac{\partial N_9^I}{\partial z} \\ \frac{\partial N_9^I}{\partial z} & 0 \\ 0 & \frac{\partial N_9^I}{\partial \rho} \\ \frac{N_9^I}{\rho} & 0 \end{bmatrix}$$

and

$$\hat{\mathbf{B}}_v = [\hat{\mathbf{B}}_v^1, \dots, \hat{\mathbf{B}}_v^9, \mathcal{S}^1 \hat{\mathbf{B}}_v^1, \dots, \mathcal{S}^9 \hat{\mathbf{B}}_v^9]_{4 \times 36} \quad (45)$$

$$\text{with } \hat{\mathbf{B}}_v^I = \left[\frac{\partial N_9^I}{\partial \rho} + \frac{N_9^I}{\rho} \frac{\partial N_9^I}{\partial z} \right]. \quad (46)$$

Appendix 4: element tangent matrix for governing equations

Using the equations of the evolution of the distribution tensor $\boldsymbol{\mu}$ (3), the components of the tangent matrix corresponding to the linear system (19) can be obtained as

$$\begin{aligned} \mathbf{K}_{vv} &= ck_B T \int_{\Omega^e} \mathbf{B}_v^T \cdot \tilde{\boldsymbol{\mu}} \cdot \mathbf{B}_v d\Omega^e \\ \mathbf{K}_{vp} &= \int_{\Omega^e} \mathbf{B}_v^T \cdot \mathbf{N}_p d\Omega^e \\ \mathbf{K}_{vp} &= \int_{\Omega^e} \mathbf{N}_p^T \cdot \hat{\mathbf{B}}_v d\Omega^e \\ \mathbf{K}_{v\bar{v}} &= \int_{\Gamma^e} \mathbf{N}_v^T \cdot \mathbf{N}_\lambda d\Gamma^e \\ \mathbf{K}_{\bar{v}} &= \int_{\Gamma^e} \mathbf{N}_\lambda^T \cdot \mathbf{N}_v d\Gamma^e \end{aligned} \quad (47)$$

and the element residual tensors

$$\begin{aligned} \mathbf{f}_v &= \int_{\Omega^e} \mathbf{B}_v^T \cdot \left[k_a \frac{C - \tilde{c}}{\tilde{c}} \mathbf{I} + k_d \boldsymbol{\mu} \right] d\Omega^e + \int_{\Gamma^e} \mathbf{N}_v^T \cdot \dot{\bar{\mathbf{t}}} d\Gamma^e \\ &\quad + \int_{\Omega^e} \mathbf{N}_v^T \cdot \dot{\mathbf{b}} d\Omega^e \\ \mathbf{f}_\lambda &= \int_{\Omega^e} \bar{\mathbf{N}}^T \cdot \bar{\mathbf{v}} d\Gamma^e. \end{aligned} \quad (48)$$

Here, we write the distribution tensor $\boldsymbol{\mu} = [\mu_{\rho\rho}, \mu_{zz}, \mu_{\rho z}, \mu_{z\rho}, \mu_{\theta\theta}]$ in Voigt notation. Accordingly, $\tilde{\boldsymbol{\mu}}$ is the distribution tensor $\boldsymbol{\mu}$ written in the Mandel form and the components in $\tilde{\boldsymbol{\mu}}$ read

$$\tilde{\boldsymbol{\mu}} = \begin{bmatrix} 2\tilde{\mu}_{\rho\rho} & 0 & 2\tilde{\mu}_{z\rho} & 0 & 0 \\ 0 & 2\tilde{\mu}_{zz} & 0 & 2\tilde{\mu}_{\rho z} & 0 \\ \tilde{\mu}_{\rho z} & \tilde{\mu}_{z\rho} & \tilde{\mu}_{zz} & \tilde{\mu}_{\rho\rho} & 0 \\ \tilde{\mu}_{\rho z} & \tilde{\mu}_{z\rho} & \tilde{\mu}_{zz} & \tilde{\mu}_{\rho\rho} & 0 \\ 0 & 0 & 0 & 0 & \tilde{\mu}_{\theta\theta} \end{bmatrix}. \quad (49)$$

In the above equations, the variables with tilde superscript ($\tilde{\cdot}$) indicate that they are interpolated using the fields from the previous timestep. We note that in many problems, the values of boundary traction $\bar{\mathbf{t}}$ and body force \mathbf{b} are usually given instead of their time derivatives $\dot{\bar{\mathbf{t}}}$ and $\dot{\mathbf{b}}$. In this case, a forward difference scheme is used for the time derivatives. For example, at time step n

$$\begin{aligned} \dot{\bar{\mathbf{t}}}_n(\mathbf{x}) &= \frac{\bar{\mathbf{t}}_{n+1}(\mathbf{x}) - \bar{\mathbf{t}}_n(\mathbf{x})}{\Delta t} \\ \dot{\mathbf{b}}_n(\mathbf{x}) &= \frac{\mathbf{b}_{n+1}(\mathbf{x}) - \mathbf{b}_n(\mathbf{x})}{\Delta t}. \end{aligned} \quad (50)$$

Appendix 5: evolution of the interface

As discussed in the text, the interface is characterized and tracked using the PMIM algorithm with the following steps: (a) *Interface initialization* At the initial time t_0 , the interface is discretized by the particles, whose position vector \mathbf{y} are chosen as the closest points from each neighboring grid nodes to the interface. The position vector \mathbf{y} can be obtained using our knowledge of initial levelset function $\phi(\mathbf{x}, t_0)$ as

$$\mathbf{y} = \mathbf{x} - \phi(\mathbf{x}, t_0) \bar{\mathbf{n}}(\mathbf{x}, t_0) \quad (51)$$

where the normal vector is obtained by $\bar{\mathbf{n}} = \nabla \phi(\mathbf{x}, t_0)$ [27] and \mathbf{x} is the position vector of the corresponding grid node. (b) *Update the interface* At an arbitrary time t , given the velocity solution of the interface velocity $\bar{\mathbf{v}}^t$, update the position of each particle by a second order Runge-Kutta scheme as

$$\begin{aligned} \mathbf{y}^{t+\frac{dt}{2}} &= \mathbf{y}^t + \bar{\mathbf{v}}(\mathbf{y}^t, t) \frac{dt}{2} + \boldsymbol{\Omega} \cdot \bar{\mathbf{v}}(\mathbf{y}^t, t) \frac{dt^2}{4} \\ \mathbf{y}^{t+dt} &= \mathbf{y}^t + \bar{\mathbf{v}}(\mathbf{y}^{t+\frac{dt}{2}}, t) \frac{dt}{2} + \boldsymbol{\Omega} \cdot \bar{\mathbf{v}}(\mathbf{y}^{t+\frac{dt}{2}}, t) \frac{dt^2}{2} \end{aligned} \quad (52)$$

where $\boldsymbol{\Omega}$ is the skew-symmetric spin tensor that reads

$$\boldsymbol{\Omega} = \begin{bmatrix} 0 & -\omega_z \\ \omega_z & 0 \end{bmatrix} \quad \text{with} \quad \omega_z = (\bar{v}_{,\xi^2}^{\parallel} - \bar{v}_{,\xi^1}^{\parallel}). \quad (53)$$

The function is then updated to account for the new geometry of the interface

$$\phi(\mathbf{y}, t + dt) = g(\mathbf{y}^{t+dt}, \mathbf{x}) |\mathbf{y}^{t+dt} - \mathbf{x}| \quad (54)$$

where $g(\mathbf{y}^{t+dt}, \mathbf{x})$ is a sign function that determines whether a point \mathbf{x} locates inside or outside of the interface

$$g(\mathbf{y}^{t+dt}, \mathbf{x}) = -\text{sgn} \left(\frac{\mathbf{y}^{t+dt} - \mathbf{x}}{|\mathbf{y}^{t+dt} - \mathbf{x}|} \cdot \bar{\mathbf{n}}^t \right). \quad (55)$$

It is clear that the function g takes the value -1 inside the vesicle, and 1 outside the vesicle.

(c) *Interface approximation* After obtaining the updated levelset function, the interface geometry is approximated using the local polynomials for each particle P . More specifically, for each particle P with position vector \mathbf{y}_p , one can introduce a local orthonormal basis that consists of tangent and normal vectors $\{\bar{\mathbf{a}}_p^{t+dt}, \bar{\mathbf{n}}_p^{t+dt}\}$ to the interface. These two quantities can be obtained from the levelset function as follows

$$\begin{aligned} \bar{\mathbf{n}}_p^{t+dt} &= \nabla \phi(\mathbf{y}_p, t + dt) \\ \bar{\mathbf{a}}_p^{t+dt} &= \bar{\mathbf{n}}_p^{t+dt} \times \mathbf{m} / |\bar{\mathbf{n}}_p^{t+dt} \times \mathbf{m}| \end{aligned} \quad (56)$$

where $\mathbf{m} = [0 \ 0 \ 1]^T$ is the unit vector normal to the computational domain. To approximate the local geometry of the interface, we collect the closest m particles in the neighborhood of P , given by their positions $\tilde{\mathbf{y}}_1 \dots \tilde{\mathbf{y}}_m$ in the local coordinates

$$\tilde{\mathbf{y}}_i = \begin{Bmatrix} \xi_i^1 \\ \xi_i^2 \end{Bmatrix} = \mathbf{R}^{t+dt} \cdot (\mathbf{y}_i - \mathbf{y}_p) \quad \text{with} \quad \mathbf{R}^{t+dt} = \begin{bmatrix} \bar{\mathbf{a}}_p^{t+dt} \\ \bar{\mathbf{n}}_p^{t+dt} \end{bmatrix} \quad (57)$$

and construct a polynomial using the least square fitting method

$$\xi^2(\xi^1) = \sum_{i=0}^n c_i (\xi^1)^i \quad (58)$$

where the coefficients c_i are determined by minimizing the L^2 difference between the approximation $\xi^2(\xi_i^1)$ and the nodal values ξ_i^2 . In this way, a local parameterization $\mathbf{r}^l(\rho, t)$ of the interface around the particle \mathbf{y}_p is achieved, whose global parameterization $\mathbf{r}(\rho, t)$ can then be obtained as

$$\mathbf{r}(\rho, t) = (\mathbf{R}^{t+dt})^{-1} \mathbf{r}^l(\xi^1, t) + \mathbf{y}_p. \quad (59)$$

Finally, the tangential and normal vectors for a point on the interface Γ can be obtained in the global coordinates as

$$\begin{aligned} \bar{\mathbf{a}}^{t+dt} &= \mathbf{r}(\rho, t + d),_{\rho} = \mathbf{R}^{t+dt} \frac{\partial \mathbf{r}^l(\xi^1, t)}{\partial \xi^1} \\ \bar{\mathbf{n}}^{t+dt} &= \bar{\mathbf{a}}^{t+dt} \times \mathbf{m} / |\bar{\mathbf{a}}^{t+dt} \times \mathbf{m}|. \end{aligned} \quad (60)$$

Appendix 6: element matrices for enriched degrees of freedom

The global tangent matrices to compute the enriched degrees of freedom $\bar{\boldsymbol{\mu}}_g^{enr}$ and $\bar{\mathbf{p}}_g^{enr}$ are written as

$$\mathbf{K}_{\boldsymbol{\mu}}^{enr} = \sum_e \int_{\Omega^e} (\mathbf{N}_{\boldsymbol{\mu}}^{enr})^T \mathbf{N}_{\boldsymbol{\mu}}^{enr} d\Omega^e \quad (61)$$

$$\mathbf{K}_{\mathbf{p}}^{enr} = \sum_e \int_{\Omega^e} (\mathbf{N}_{\mathbf{p}}^{enr})^T \mathbf{N}_{\mathbf{p}}^{enr} d\Omega^e \quad (62)$$

and the residue vector is given by

$$\begin{aligned} \mathbf{R}_{\boldsymbol{\mu}}^{enr} &= \sum_e \int_{\Omega^e} (\mathbf{N}_{\boldsymbol{\mu}}^{enr})^T (\tilde{\boldsymbol{\mu}} - \mathbf{N}_{\boldsymbol{\mu}}^{reg} \boldsymbol{\mu}^{reg}) d\Omega^e \\ \mathbf{R}_{\mathbf{p}}^{enr} &= \sum_e \int_{\Omega^e} (\mathbf{N}_{\mathbf{p}}^{enr})^T (\tilde{\mathbf{p}} - \mathbf{N}_{\mathbf{p}}^{reg} \mathbf{p}^{reg}) d\Omega^e. \end{aligned} \quad (63)$$

In the above equations \sum_e indicates the matrix assembly of the global system from the element matrices.

References

- Akalp U, Bryant SJ, Vernerey FJ (2016) Tuning tissue growth with scaffold degradation in enzyme-sensitive hydrogels: a mathematical model. *Soft Matter* 12(36):7505–7520
- Asbury JB, Steinel T, Fayer MD (2004) Hydrogen bond networks: structure and evolution after hydrogen bond breaking. *J Phys Chem B* 108(21):6544–6554
- Bathe K-J (2001) The inf-sup condition and its evaluation for mixed finite element methods. *Comput Struct* 79(2):243–252
- Bathe K-J (2006) Finite element procedures. Prentice-Hall, Upper Saddle River
- Bathe K-J, Wilson EL (1976) Numerical methods in finite element analysis, vol 197. Prentice-Hall, Upper Saddle River
- Benet E, Vernerey FJ (2016) Mechanics and stability of vesicles and droplets in confined spaces. *Phys Rev E* 94(6):062613
- Benson DJ (1992) Computational methods in lagrangian and eulerian hydrocodes. *Comput Methods Appl Mech Eng* 99(2–3):235–394
- Bergström JS, Boyce MC (2001) Constitutive modeling of the time-dependent and cyclic loading of elastomers and application to soft biological tissues. *Mech Mater* 33(9):523–530
- Chapelle D, Bathe K-J (1993) The inf-sup test. *Comput Struct* 47(4–5):537–545
- Chia HN, Wu BM (2015) Recent advances in 3D printing of biomaterials. *J Biol Eng* 9(1):4
- Choi YJ, Hulsén MA (2012) Alignment of particles in a confined shear flow of a viscoelastic fluid. *J Non-Newton Fluid Mech* 175:89–103
- Choi Y, Hulsén MA, Meijer HEH (2010) An extended finite element method for the simulation of particulate viscoelastic flows. *J Non-Newton Fluid Mech* 165(11–12):607–624
- Choi YJ, Hulsén MA, Meijer HEH (2012) Simulation of the flow of a viscoelastic fluid around a stationary cylinder using an extended finite element method. *Comput Fluids* 57:183–194
- Christensen RM, Freund LB (1971) Theory of viscoelasticity. *J Appl Mech* 38:720
- De Gennes PG, Leger L (1982) Dynamics of entangled polymer chains. *Ann Rev Phys Chem* 33(1):49–61
- de Gennes PG (1992) Reptation of a polymer chain in the presence of fixed obstacles. *Simple Views Condens Matter* 4:148
- Doi M (2013) Soft matter physics. Oxford University Press, Oxford
- Donea J, Giuliani S, Halleux J-P (1982) An arbitrary Lagrangian–Eulerian finite element method for transient dynamic fluid–structure interactions. *Comput Methods Appl Mech Eng* 33(1–3):689–723
- Dowling NE (2012) Mechanical behavior of materials: engineering methods for deformation, fracture, and fatigue. Pearson, Pearson
- Duddu R, Lavier LL, Hughes TJR, Calo VM (2012) A finite strain Eulerian formulation for compressible and nearly incompressible hyperelasticity using high-order b-spline finite elements. *Int J Numer Methods Eng* 89(6):762–785
- Étienne J, Hinch EJ, Li J (2006) A Lagrangian–Eulerian approach for the numerical simulation of free-surface flow of a viscoelastic material. *J Non-Newton Fluid Mech* 136(2–3):157–166
- Fakhouri S, Hutchens SB, Crosby AJ (2015) Puncture mechanics of soft solids. *Soft Matter* 11(23):4723–4730
- Farsad M, Vernerey FJ (2012) An XFEM-based numerical strategy to model mechanical interactions between biological cells and a deformable substrate. *Int J Numer Methods Eng* 92(3):238–267
- Farsad M, Vernerey FJ, Park HS (2010) An extended finite element/level set method to study surface effects on the mechanical behavior and properties of nanomaterials. *Int J Numer Methods Eng* 84(12):1466–1489
- Foucard L, Aryal A, Duddu R, Vernerey F (2015) A coupled Eulerian–Lagrangian extended finite element formulation for simulating large deformations in hyperelastic media with moving free boundaries. *Comput Methods Appl Mech Eng* 283:280–302
- Foucard L, Vernerey FJ, and (2016) A particle-based moving interface method (PMIM) for modeling the large deformation of boundaries in soft matter systems. *Int J Numer Methods Eng* 107(11):923–946
- Foucard LC, Pellegrino J, Vernerey FJ (2014) Particle-based moving interface method for the study of the interaction between soft colloid particles and immersed fibrous network. *Comput Model Eng Sci* 98(1):101–127
- Foucard LC, Vernerey FJ (2015) An X-FEM-based numerical-asymptotic expansion for simulating a stokes flow near a sharp corner. *Int J Numer Methods Eng* 102(2):79–98
- Fourche G (1995) An overview of the basic aspects of polymer adhesion. Part i: fundamentals. *Polym Eng Sci* 35(12):957–967
- Gent AN, Lindley PB (1959) Internal rupture of bonded rubber cylinders in tension. In: *Proceedings of the royal society of London A: mathematical, physical and engineering sciences*, vol 249. The Royal Society, pp 195–205
- Grillet AM, Wyatt NB, Gloe LM (2012) Polymer gel rheology and adhesion. In: *Rheology*. InTech
- Hager MD, Greil P, Leyens C, van der Zwaag S, Schubert US (2010) Self-healing materials. *Adv Mater* 22(47):5424–5430
- Harlen OG, Rallison JM, Szabo P (1995) A split Lagrangian–Eulerian method for simulating transient viscoelastic flows. *J Non-Newton Fluid Mech* 60(1):81–104
- Holzappel GA (2002) Nonlinear solid mechanics: a continuum approach for engineering science. *Meccanica* 37(4):489–490
- Holzappel GA, Gasser TC (2001) A viscoelastic model for fiber-reinforced composites at finite strains: continuum basis, computational aspects and applications. *Comput Methods Appl Mech Eng* 190(34):4379–4403
- Hughes TJR, Liu WK, Zimmermann TK (1981) Lagrangian–Eulerian finite element formulation for incompressible viscous flows. *Comput Methods Appl Mech Eng* 29(3):329–349
- Kalcioglu ZI, Mahmoodian R, Hu Y, Suo Z, Van Vliet KJ (2012) From macro-to microscale poroelastic characterization of polymeric hydrogels via indentation. *Soft Matter* 8(12):3393–3398
- Kloxin CJ, Bowman CN (2013) Covalent adaptable networks: smart, reconfigurable and responsive network systems. *Chem Soc Rev* 42(17):7161–7173
- Le Tallec P, Rahier C, Kaiss A (1993) Three-dimensional incompressible viscoelasticity in large strains: formulation and numerical approximation. *Comput Methods Appl Mech Eng* 109(3–4):233–258
- Leung S, Lowengrub J, Zhao H (2011) A grid based particle method for solving partial differential equations on evolving surfaces and modeling high order geometrical motion. *J Comput Phys* 230(7):2540–2561
- Leung S, Zhao H (2009) A grid based particle method for moving interface problems. *J Comput Phys* 228(8):2993–3024
- Lin DC, Yurke B, Langrana NA (2004) Mechanical properties of a reversible, DNA-crosslinked polyacrylamide hydrogel. *J Biomech Eng* 126(1):104–110
- Lipson H, Kurman M (2013) Fabricated: the new world of 3D printing. Wiley, Hoboken
- Liu X, Fernandes R, Jurisicova A, Casper RF, Sun Y (2010) In situ mechanical characterization of mouse oocytes using a cell holding device. *Lab Chip* 10(16):2154–2161
- Liu X, Shi J, Zong Z, Wan K-T, Sun Y (2012) Elastic and viscoelastic characterization of mouse oocytes using micropipette indentation. *Ann Biomed Eng* 40(10):2122–2130

46. Long R, Hui C-Y (2010) Effects of triaxiality on the growth of crack-like cavities in soft incompressible elastic solids. *Soft Matter* 6(6):1238–1245
47. Lubliner J (1985) A model of rubber viscoelasticity. *Mech Res Commun* 12(2):93–99
48. Maeda T, Otsuka H, Takahara A (2009) Dynamic covalent polymers: reorganizable polymers with dynamic covalent bonds. *Prog Polym Sci* 34(7):581–604
49. Miehe C, Göktepe S, Lulei F (2004) A micro-macro approach to rubber-like materials. Part i: the non-affine micro-sphere model of rubber elasticity. *J Mech Phys Solids* 52(11):2617–2660
50. Miehe C, Göktepe S (2005) A micro-macro approach to rubber-like materials. Part ii: the micro-sphere model of finite rubber viscoelasticity. *J Mech Phys Solids* 53(10):2231–2258
51. Moës N, Béchet E, Tourbier M (2006) Imposing dirichlet boundary conditions in the extended finite element method. *Int J Numer Methods Eng* 67(12):1641–1669
52. Moës N, Belytschko T (2002) Extended finite element method for cohesive crack growth. *Eng Fract Mech* 69(7):813–833
53. Nanthakumar SS, Lahmer T, Zhuang X, Park HS, Rabczuk T (2016) Topology optimization of piezoelectric nanostructures. *J Mech Phys Solids* 94:316–335
54. Plohr BJ, Sharp DH (1988) A conservative Eulerian formulation of the equations for elastic flow. *Adv Appl Math* 9(4):481–499
55. Quadrini F, Squeo EA, Guglielmotti A (2010) Indentation creep of polymers. i. Experimental. *Polym Eng Sci* 50(12):2431–2439
56. Rasmussen HK (1999) Time-dependent finite-element method for the simulation of three-dimensional viscoelastic flow with integral models. *J Non-Newton Fluid Mech* 84(2–3):217–232
57. Reese S, Govindjee S (1998) A theory of finite viscoelasticity and numerical aspects. *Int J Solids Struct* 35(26–27):3455–3482
58. Shaw MT, MacKnight WJ (2005) Introduction to polymer viscoelasticity. Wiley, Hoboken
59. Shen T, Vernerey F (2017) Phoretic motion of soft vesicles and droplets: an XFEM/particle-based numerical solution. *Comput Mech* 60(1):143–161
60. Simo JC (1987) On a fully three-dimensional finite-strain viscoelastic damage model: formulation and computational aspects. *Comput Methods Appl Mech Eng* 60(2):153–173
61. Sridhar SL, Schneider MC, Chu S, de Roucy G, Bryant SJ, Vernerey FJ (2017) Heterogeneity is key to hydrogel-based cartilage tissue regeneration. *Soft Matter* 13(28):4841–4855
62. Stolarska M, Chopp DL, Moës N, Belytschko T (2001) Modelling crack growth by level sets in the extended finite element method. *Int J Numer Methods Eng* 51(8):943–960
63. Style RW, Boltyanskiy R, Allen B, Jensen KE, Foote HP, Wettlaufer JS, Dufresne ER (2014) Stiffening solids with liquid inclusions. *arXiv preprint [arXiv:1407.6424](https://arxiv.org/abs/1407.6424)*
64. Sukumar N, Chopp DL, Moës N, Belytschko T (2001) Modeling holes and inclusions by level sets in the extended finite-element method. *Comput Methods Appl Mech Eng* 190(46):6183–6200
65. Takashi N, Hughes TJR (1992) An arbitrary Lagrangian–Eulerian finite element method for interaction of fluid and a rigid body. *Comput Methods Appl Mech Eng* 95(1):115–138
66. Tanaka F, Edwards SF (1992) Viscoelastic properties of physically crosslinked networks. I. Transient network theory. *Macromolecules* 25(5):1516–1523
67. Tezduyar TE, Behr M, Mittal S, Liou J (1992) A new strategy for finite element computations involving moving boundaries and interfaces the deforming-spatial-domain/space–time procedure: ii. Computation of free-surface flows, two-liquid flows, and flows with drifting cylinders. *Comput Methods Appl Mech Eng* 94(3):353–371
68. Treloar LRG (1943) The elasticity of a network of long-chain molecules ii. *Trans Faraday Soc* 39:241–246
69. Tvergaard V, Needleman A (2011) Polymer indentation: numerical analysis and comparison with a spherical cavity model. *J Mech Phys Solids* 59(9):1669–1684
70. Vernerey FJ (2018) Transient response of nonlinear polymer networks: a kinetic theory. *J Mech Phys Solids* 115:230–247
71. Vernerey FJ, Akalp U (2016) Role of catch bonds in actomyosin mechanics and cell mechanosensitivity. *Phys Rev E* 94(1):012403
72. Vernerey FJ, Farsad M (2011) A constrained mixture approach to mechano-sensing and force generation in contractile cells. *J Mech Behav Biomed Mater* 4(8):1683–1699
73. Vernerey FJ, Kabiri M (2012) An adaptive concurrent multiscale method for microstructured elastic solids. *Comput Methods Appl Mech Eng* 241:52–64
74. Vernerey FJ, Long R, Brighenti R (2017) A statistically-based continuum theory for polymers with transient networks. *J Mech Phys Solids* 107:1–20
75. Vitali E, Benson DJ (2006) An extended finite element formulation for contact in multi-material arbitrary Lagrangian–Eulerian calculations. *Int J Numeric Methods Eng* 67(10):1420–1444
76. Vu-Bac N, Bessa MA, Rabczuk T, Liu WK (2015) A multiscale model for the quasi-static thermo-plastic behavior of highly cross-linked glassy polymers. *Macromolecules* 48(18):6713–6723
77. Wojtecki RJ, Meador MA, Rowan SJ (2011) Using the dynamic bond to access macroscopically responsive structurally dynamic polymers. *Nat Mater* 10(1):14
78. Yamamoto M (1956) The visco-elastic properties of network structure i. General formalism. *J Phys Soc Jpn* 11(4):413–421
79. Zhu J, Li T, Cai S, Suo Z (2011) Snap-through expansion of a gas bubble in an elastomer. *J Adhes* 87(5):466–481
80. Zienkiewicz OC, Taylor RL, Zienkiewicz OC, Taylor RL (1977) The finite element method, vol 3. McGraw-Hill, London
81. Zimmerlin JA, McManus JJ, Crosby AJ (2010) Cavitation rheology of the vitreous: mechanical properties of biological tissue. *Soft Matter* 6(15):3632–3635
82. Zimmerlin JA, Sanabria-DeLong N, Tew GN, Crosby AJ (2007) Cavitation rheology for soft materials. *Soft Matter* 3(6):763–767